

# Measurement of Tagged Deep Inelastic Scattering (TDIS)

June 2, 2014

A. Camsonne, D. Gaskell, D. Higinbotham, M. Jones, C. E. Keppel (Spokesperson)<sup>1</sup>,  
W. Melnitchouk, C. Weiss, B. Wojtsekhowski (Spokesperson)  
*JEFFERSON LAB*

R. Holt, P. Reimer  
*ARGONNE NATIONAL LAB*

P. King (Spokesperson), J. Roche  
*OHIO UNIVERSITY*

J. Dunne, D. Dutta (Spokesperson), A. Narayan,  
L. Ndukum, A. Subedi, and L. Ye  
*MISSISSIPPI STATE UNIVERSITY*

C. Hyde, S. Kuhn, L. Weinstein  
*OLD DOMINION UNIVERSITY*

J. R. M. Annand (Spokesperson)  
*UNIVERSITY OF GLASGOW*

J.-C. Peng  
*UNIVERSITY OF ILLINOIS AT URBANA CHAMPAIGN*

G. Cates, K. Gnanvo, R. Lindgren, N. Liyanage, J. Zhang (Spokesperson)  
*UNIVERSITY OF VIRGINIA*

T. Averett, K. Griffioen  
*COLLEGE OF WILLIAM AND MARY*

T. Hobbs, T. Londergan  
*INDIANA UNIVERSITY*

---

<sup>1</sup>Contact person

X. Jiang  
*LOS ALAMOS NATIONAL LABORATORY*

M.E. Christy, N. Kalantarians, M. Kohl, P. Monaghan, L.Tang  
*HAMPTON UNIVERSITY*

I. Niculescu, G. Niculescu  
*JAMES MADISON UNIVERSITY*

## Abstract

We propose to investigate tagged deep inelastic scattering (TDIS) by measuring high  $W^2$ ,  $Q^2$  electrons scattered from hydrogen and deuterium targets in coincidence with low momentum recoiling protons. This is a pioneering experiment that will probe the elusive mesonic content of the nucleon, using the tagging technique to isolate for example scattering from the pion in proton to pion fluctuations. It will thereby directly measure hadron production in the *target* fragmentation region and the fracture functions. At (extrapolated) low values of  $t$ , this approach will also provide access to the pion structure function via the Sullivan process.

The experiment utilizes the Hall A Super BigBite spectrometer for electron detection, in conjunction with the thin target, solenoid and GEM-based radial time projection chamber approach that was realized in experiments such as BONUS and eg6 for low momentum spectator tagging. These combined systems, along with the CEBAF high current CW beam, leverage the high luminosity and unique kinematics required to access the proposed physics. The low momentum tagging technique will reduce backgrounds from both experimental and theoretically competing processes, enhancing isolation of the electron-meson scattering events.

# Contents

<b>1</b>	<b>Physics Motivation</b>	<b>5</b>
1.1	Fracture Functions and Conditional Parton Distribution Functions . . . . .	6
1.2	Tagged Deep Inelastic Scattering (TDIS) . . . . .	12
1.2.1	Meson Cloud Contributions to Inclusive DIS . . . . .	12
1.2.2	Tagged Structure Functions . . . . .	14
1.3	Measurement of the Pion Structure Function via the Sullivan Process . . .	23
1.4	Impact for the Jefferson Lab 12 GeV Program and Beyond . . . . .	29
1.5	Physics Motivation Summary . . . . .	30
<b>2</b>	<b>Experiment</b>	<b>32</b>
2.1	Overview . . . . .	32
2.2	Experiment Luminosity . . . . .	32
2.3	Recoil Detector . . . . .	36
2.3.1	Target cell . . . . .	39
2.3.2	RTPC Calibration . . . . .	40
2.4	The Super Bigbite Spectrometer . . . . .	41
2.4.1	CLAS6 Large Acceptance Calorimeter . . . . .	44
2.4.2	Super Bigbite Trigger and DAQ . . . . .	45
2.5	Simulations of the Radial Time Project Chamber . . . . .	46
2.5.1	Kinematics . . . . .	52
<b>3</b>	<b>Projected Results</b>	<b>53</b>
3.1	Beam Time Request . . . . .	55
3.2	Expected Experimental Accuracy . . . . .	57
<b>4</b>	<b>Summary</b>	<b>58</b>

# 1 Physics Motivation

The concept of a composite nucleon structure may be tracked as far back as 1933 to the discovery of the anomalous magnetic moment of the proton [1]. This was explicitly formulated by Fermi and Marshall who noted in a 1947 paper [2] that experimental evidence pointed to the nucleon existing approximately 20% of the time in a virtual meson-nucleon state. The virtual meson "cloud" of the nucleon plays an important role in the understanding of the nucleon-nucleon interaction and the pion cloud in particular has always been considered critical to understanding the nucleon's long-range structure. At shorter ranges, the role of mesons in electron-nucleon deep inelastic scattering (DIS) have also been investigated. In 1972 Sullivan [3] suggested that some fraction of the nucleon's anti-quark sea distribution may be associated with this pion content of the nucleon. For many decades these and numerous other theories that describe and/or utilize the meson cloud of the nucleon have advanced significantly (see [4, 5, 6] for some review). From partially conserved axial current to the success of chiral quark models, it is considered known that the nucleon has an associated meson cloud. In very stark contrast to the substantial body of theory associated with the cloud, however, experimental results remain few and far between. In a 1983 paper, Thomas commented that "...it is rather disturbing that no one has yet provided direct experimental evidence of a pionic component in the nucleon" [7]. Even with some results becoming available from Drell-Yan experiments at Fermilab, W production at RHIC, and diffractive DIS at HERA and COMPASS, all discussed below, the "disturbing" situation is not much different today.

The physics motivation for this experiment is, then, basically this: to pioneer a measurement technique probing the elusive mesonic content of the nucleon structure function. There is vibrant interest in this physics, as evidenced by two workshops this past year on the topic, "Flavor Structure of the Nucleon Sea", held in July 2013 in Trento, Italy and "Exploring Hadron Structure with Tagged Structure Functions", held in January 2014 at Jefferson Lab. Collaborations have attempted proposals, but have been hindered largely by lack of low momentum reach, large backgrounds, or both [8].

To motivate the measurement, we begin with the fracture function formalism which provides a QCD framework for the target fragmentation region (1.1), then turn to a description of the kinematics and predictions for the mesonic component of the nucleon structure function (1.2), and move to an extension of the experiment to extract the pion structure function via the Sullivan process (1.3). Lastly, we discuss the broader impact of the experiment (1.4), and summarize the multiple motivations in (1.5). These sections follow.

## 1.1 Fracture Functions and Conditional Parton Distribution Functions

Deep-inelastic electron–nucleon scattering (DIS) has been one of the principal sources of information about the dynamics of strong interactions at distances  $\ll 1$  fm and the internal structure of the nucleon. In the simplest case such experiments measure the *inclusive* cross section  $eN \rightarrow e'X$  in the region of large energies and momentum transfers,  $W^2, Q^2 \gg 1 \text{ GeV}^2$ . Thanks to the asymptotic freedom of QCD this cross section can be factorized into the cross section for scattering from a quasi-free parton (quark, antiquark), which takes place over distances  $\sim 1/Q$  and is calculable using perturbation theory, and the so-called parton density, which describes the light-cone momentum distribution of the quarks and antiquarks in the nucleon, as arising from non-perturbative dynamics at distances  $\sim 1$  fm (see Fig. 1a,b). The parton densities are rigorously defined as nucleon matrix elements of certain QCD composite operators and can be calculated using non-perturbative methods such as Lattice QCD. QCD radiation (bremsstrahlung with momenta ranging up to  $\sim Q$ ) leads to an effective logarithmic dependence of the parton densities on  $Q^2$ , described in a simple way through evolution equations (DGLAP).

An important consequence of factorization is that the parton densities do not depend on the specific scattering process used to measure them; e.g., the same densities appear also in neutrino-induced DIS, Drell-Yan pair production in  $pp$  collisions, jet production, etc. This “*universality*” ensures that the parton densities are objective measures of nucleon structure in QCD. Considerable efforts have been devoted to extracting the parton densities from fits to data from various high-energy scattering processes. The results of these fits have provided many interesting insights into nucleon structure, such as the presence of a non-perturbative flavor-asymmetric “sea” of antiquarks at the hadronic scale [25, 26]; a large non-perturbative density of gluons [27, 28, 29], and the distribution of the nucleon spin over its quark and gluon constituents [30, 31]. Experiments with the JLab 12 GeV Upgrade will provide crucial new information about the parton densities at large light-cone momentum fractions  $x \rightarrow 1$  and the spin distributions [32].

Much more information about nucleon structure and QCD dynamics can be gained from measurements of DIS with *identified hadrons* in the final state,  $eN \rightarrow e' + h + X'$ . The final state in DIS measurement is generally divided into three regions: (a) the current fragmentation region, containing hadrons produced by fragmentation of the struck quark; (b) the target fragmentation region, containing hadrons produced in the breakup of the target nucleon; and (c) a central region, populated by hadrons produced through QCD radiation and/or hadronization of small- $x$  partons. The precise identification of these regions depends on the variables used to characterize the final state (rapidity, energy fraction  $z$ , Feynman variable  $x_F$ ), and different conventions are used in the literature. In DIS experiments at JLab with 11 GeV energy it is generally expected that a reasonable separation of current and target fragmentation regions can be achieved using the standard criteria (e.g.  $x_F < 0$  and  $> 0$ ); a central region is absent because of the limited energy. An extensive program of DIS experiments in the current fragmentation region (semi-inclusive DIS) is planned with 11 GeV, with the aim to measure the flavor structure of the nucleon and certain transverse momentum-dependent distributions of quarks (TMDs).

Equally — and in some respects even more — interesting is the study of hadron

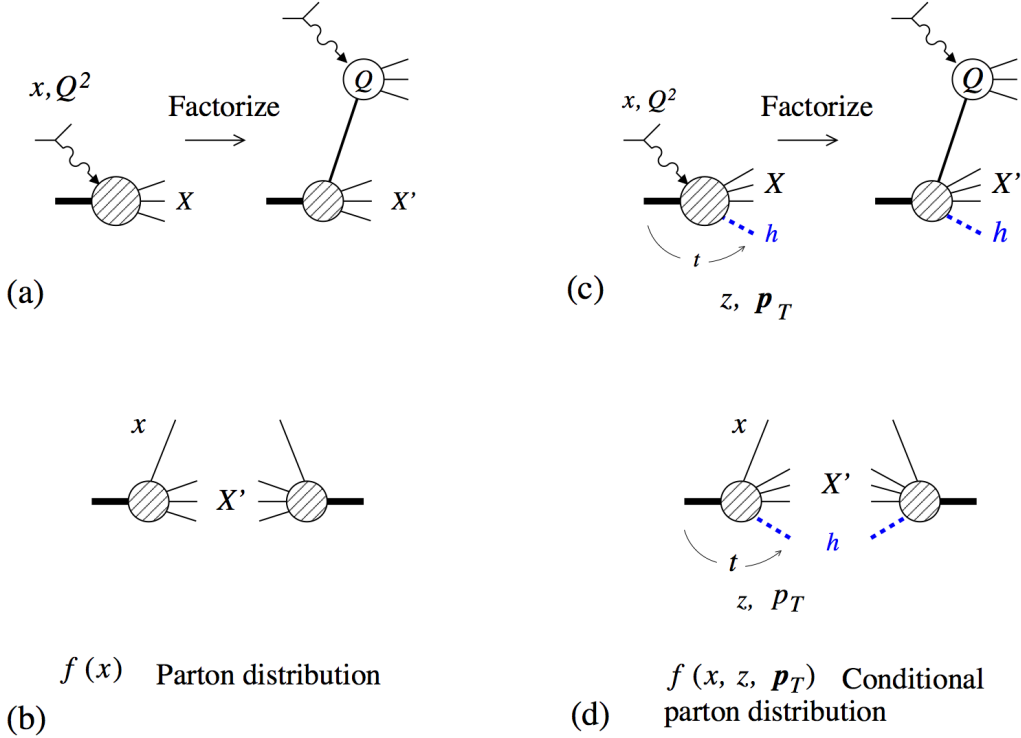


Figure 1: Factorization in deep-inelastic scattering. (a) Inclusive DIS  $eN \rightarrow e' + X$ . The scattering process takes place on a quark in the target (b) Parton distribution  $f(x)$ . It describes the probability distribution of quarks with respect to their light-cone momentum fraction  $x$  in the target (c) Conditional cross section with an identified hadron in the target fragmentation region  $eN \rightarrow e' + h(\text{target}) + X$ . Factorization is performed in analogy to the inclusive case. (d) Conditional parton distribution. It describes the probability to find a hadron  $h$  in the target fragmentation region, with light-cone momentum fraction  $1 - z$  and transverse momentum  $\mathbf{p}_T$ , after removing a quark with light-cone momentum fraction  $x$ .

production in the target fragmentation of DIS,  $eN \rightarrow e' + h(\text{target region}) + X'$ , which represents a particular conditional case of inclusive DIS. QCD factorization for the single-hadron inclusive cross section in this region was proved in Refs. [42, 34] and proceeds along the same lines as for fully inclusive scattering, with the hard parton-level process the same as in the inclusive case (see Fig. 1c). Bjorken scaling of the cross section for a fixed hadron momentum  $|\mathbf{p}_h| \ll Q$  (in the target rest frame) is expected to occur on the same grounds as in inclusive scattering and serves as a powerful test of the production mechanism. The partonic structure of the target is now described by a *conditional parton distribution* (or fracture function) which depends not only on the light-cone momentum fraction of the parton,  $x$ , but also on the momentum of the produced hadron in the target fragmentation region, usually described by the variables

$$1 - z \equiv \frac{p_h^+}{P^+} \quad \text{Light-cone momentum fraction of observed hadron, } z > x \quad (1)$$

$$p_{Th} \equiv |\mathbf{p}_{Th}| \quad \text{Transverse momentum of observed hadron}$$

Alternatively, one uses the invariant momentum transfer between the target nucleon and the produced hadron, defined as

$$t \equiv (p_h - p_N)^2 \quad (2)$$

The conditional parton distribution  $f_q(x, z, t)$  describes the probability to find a hadron  $h$  with light-cone momentum  $z$  and  $p_T$  in the nucleon *after removing* a quark of type  $q$  with light-cone momentum fraction  $x$  (see Fig. 1d). Just as the usual parton densities, they are independent of the hard scattering process that removed the parton and represent the objective structure of the target. The conditional parton densities at fixed hadron momentum obey the *same* QCD evolution equations as the usual PDFs,<sup>2</sup> allowing one to compute their scale dependence from first principles and compare results of experiments at different  $Q^2$ .

The conditional PDFs contain a wealth of interesting information about nucleon structure and non-perturbative dynamics. Different physical interpretations are being considered in different regions of the parton momentum fractions  $x$ :

- At  $x \ll 1$  the conditional PDFs for nucleon production in the target fragmentation region ( $h = p, n$ ) describe the partonic content of the “meson-like” system exchanged between the target nucleon and the operator measuring the parton density ( $t$ -channel picture). Depending on the energy region and the quantum numbers this can be a Regge trajectory, a single meson, or a multi-meson state. Particularly interesting examples are

$$p \rightarrow p, \quad x \ll 0.1 \quad \text{Pomeron exchange} \quad (3)$$

$$p \rightarrow n \text{ or } n \rightarrow p, \quad x \sim 0.1 \quad \text{Charged pion exchange} \quad (4)$$

---

<sup>2</sup>Some authors consider the conditional parton densities integrated over the hadron transverse momenta (fracture functions) [42]. Their QCD evolution equation differs from the standard DGLAP equations by an inhomogeneous term, which describes the feed-down of hadrons produced by fragmentation of partons appearing through QCD radiation [42]. Here we consider the conditional parton densities at fixed momenta  $p_{Th} \ll Q$ , for which this effect is parametrically suppressed, and which obey the usual DGLAP evolution equations [34].



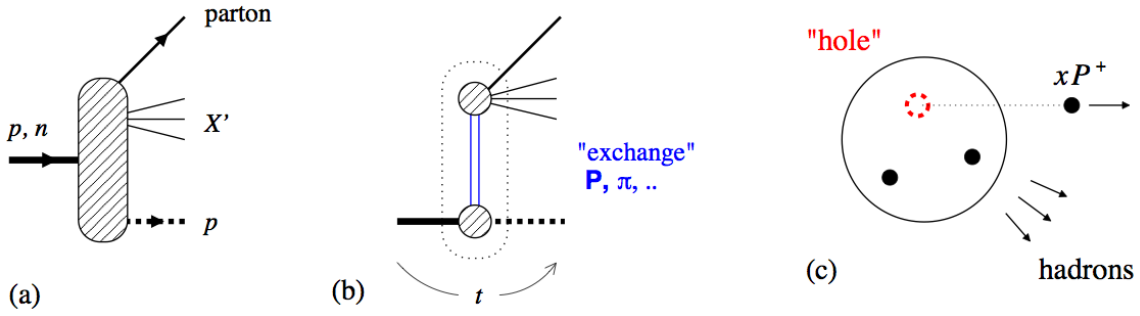


Figure 2: (a) Conditional PDF for production of a nucleon (proton) in the target fragmentation region. (b) Interpretation in terms of  $t$ -channel exchange at  $x \ll 0.1$ . (c) Interpretation as materialization of nucleon remnant with hole in the valence-quark dominated region  $x > 0.3$ .

The conditional PDF in these regions is given by the product of the light-cone momentum distribution of the exchanged system (“flux”) and the parton density of the exchanged system. The channel Eq. (3) was explored at HERA and gave rise to a very successful description of conditional PDFs in terms of the partonic content of the Pomeron [36, 37, 38]. The channel Eq. (4) represents a unique method for measuring the parton distributions of the pion and will be explored in the present experiment (see below) [36]. The pionic contribution to the conditional PDF can be rigorously identified by extrapolating in the variable  $t$  to the pole at  $t = M_\pi^2$  (unphysical region).

- In the region  $x > 0.3$  the DIS process on the nucleon predominantly “knocks out” a valence quark, leaving behind a system with a “hole” in the color/spin/flavor wave function. Production of hadrons in the target fragmentation region reveals how such a system with a hole materializes in physical hadrons. This represents a fundamental process of QCD and provides important information about non-perturbative dynamics, such as the role of dynamical chiral symmetry breaking (constituent quarks as effective degrees of freedom, short-range non-perturbative forces) and color confinement in hadron formation. It also provides new insight into nucleon structure, as the hadronization process is sensitive to the isospin (flavor structure) and spin of the initial nucleon and produced hadron system. Target fragmentation in this region of  $x$  is largely unexplored and remains a major potential source of information on nucleon structure.

Here we propose a pioneering measurement of conditional DIS with nucleon production in the target fragmentation region using the JLab 11 GeV electron beam, the Hall A Super BigBite spectrometer for electron detection, and a dedicated time projection chamber for recoil proton tagging. The conditional cross section for proton production will for the first time be measured both for a proton *and a neutron target*,  $e+p$  (or  $n$ )  $\rightarrow e'+p+X$ ; the latter channel will be identified using an innovative method of scattering from a deuterium target and tagging two low-momentum recoil protons at backward angles,  $eD \rightarrow e' + p + p + X$ . The objectives of this experiment are:

- I) Establish the QCD-based reaction mechanism for nucleon production in the target fragmentation region at JLab energies by testing model-independent features such as Bjorken scaling at fixed recoil momentum ( $z, t$ ), and investigating the kinematic dependences;
- II) Measure the conditional PDFs for both  $p \rightarrow p$  and  $p \rightarrow n$  transitions, particularly their isospin dependence, compare it with dynamical models and measurements at higher energies (COMPASS, HERA) using DGLAP evolution;
- III) Extract the pion exchange contribution to the conditional PDFs and relate it to the parton density of the pion, as measured also in other reactions (Drell-Yan pair production in  $\pi A$  scattering), testing its universality and providing new information about its strength at large values of  $x/z$  (quark/antiquark momentum fraction in pion).

Measurements of proton and neutron production in the target region have been performed at the HERA collider at  $x < 10^{-2}$ . Target fragmentation into baryons, especially  $\Lambda$  hyperons (whose spin polarization can be detected through their decay), is also measured at the CERN COMPASS experiment [35]. Nucleon production in the valence region  $x > 0.1$  remains unexplored and would for the first time be measured in the JLab12 experiment. The proposed experiment is thus complementary to the existing measurements and would substantially broaden our knowledge of target fragmentation. The projected results can be related to the high-energy measurements through DGLAP evolution, testing the universality of the conditional PDFs. It is important to note that the data from high-energy experiments such as COMPASS are at *both higher  $Q^2$  and smaller  $x$*  — exactly the region connected to the JLab region by the evolution flow. In particular, the measurement of the isospin dependence ( $p$ - $n$  difference) of the conditional PDFs would settle the question of the relative importance of singlet and non-singlet exchanges in target fragmentation, which cannot be answered from the high-energy data alone.

Measurements of the  $n \rightarrow p$  conditional PDF represent a clean (parametrically controlled) method for probing the partonic content of the nucleon's pion cloud in inclusive scattering and extracting information about the pion PDF. Taking advantage of the additional kinematic variable  $t$ , the pionic contribution to the conditional PDF can be rigorously defined as the residue of the pole at  $t = M_\pi^2$ , which can be extracted from the data by extrapolating to the unphysical region. The physical region of  $t$  in conditional DIS with a nucleon in the target fragmentation region is

$$-t > -t_{\min} \equiv \frac{z^2 M_N^2}{1 - z}, \quad z > x, \quad (5)$$

where  $z$  is the pion light-cone momentum fraction in the nucleon. In DIS measurements at JLab energy the kinematically accessible values of  $t$  are rather large,  $-t > 0.1 \text{ GeV}^2$  for  $x \sim 0.3$ , so that one cannot rely on dominance of the pion pole alone but has to use dynamical models to separate pole and non-pole (background) contributions. Even so, measurements of the conditional PDFs can constrain the parton densities of the pion and provide interesting information about non-perturbative dynamics.

In the kinematic range accessible with JLab at 11 GeV the interpretation of hadron production in the target fragmentation region is in several ways simpler than that of semi-inclusive DIS in the current fragmentation region, which is widely discussed as a possible way to probe the transverse momentum-dependent (TMD) quark distributions in the nucleon [32]. In current fragmentation one aims to extract the transverse momentum distribution of *partons* relative to the target hadron, which can be inferred only indirectly through the hadronic jet (broadening by the transverse momentum of the hadronization process) and is affected in a complex manner by QCD radiation (Sudakov-suppressed evolution).

In contrast, target fragmentation we measure the longitudinal and transverse momentum of an identified *hadron* relative to the target hadron, which is directly observable and can be interpreted in terms of nucleon structure; e.g., it provides the invariant  $t$  which allows one to isolate definite exchange mechanisms. The QCD evolution of the conditional PDFs is the standard DGLAP evolution, which has been tested extensively in inclusive DIS and shown to work reliably down to the scales  $Q^2 \sim \text{few GeV}^2$  accessible at JLab. Finally, since at JLab energies the current and target fragmentation regions are not widely separated, a quantitative understanding of target fragmentation (longitudinal and transverse momentum distribution of target hadrons) will be a prerequisite also for the analysis of semi-inclusive DIS in the current fragmentation region.

## 1.2 Tagged Deep Inelastic Scattering (TDIS)

In specific regions of kinematics, the observation of low-momentum recoil protons in the semi-inclusive reaction  $eN \rightarrow eNX$  can reveal features associated with correlated  $q\bar{q}$  pairs in the nucleon, sometimes referred to as the nucleon's "pion cloud". In particular, at low values of the four-momentum transfer squared  $t \equiv k^2 = (p - p')^2$ , where  $p$  and  $p'$  are the initial and final nucleon four-momenta, the cross section displays behavior characteristic of pion pole dominance. Here, the contributions from the exchange of non-pseudoscalar quantum numbers ( $J^P = 0^-$ ), such as the vector  $\rho$  and  $\omega$  mesons, is suppressed. Furthermore, the direct fragmentation of the scattered quark, or spectator "diquark" system that remains after a quark is pulled out of the nucleon, generally produces a considerably more flat  $t$  dependence that is qualitatively different from that arising from the pion pole.

Here we review the predictions of pion cloud models for contributions to the structure functions of the nucleon, firstly for the inclusive DIS case, and then to the "tagged" semi-inclusive cross sections, which we study as a function of several kinematic variables [9, 10, 11]. These studies form the basis for the expected experimental results, rates, and beam time request.

### 1.2.1 Meson Cloud Contributions to Inclusive DIS

As pointed out by Sullivan [12], the contribution to the inclusive  $F_2$  structure function of the nucleon from scattering off a virtual pion emitted from the nucleon can be written as

$$F_2^{(\pi N)}(x) = \int_x^1 dz f_{\pi N}(z) F_{2\pi}\left(\frac{x}{z}\right), \quad (6)$$

where  $z = k^+/p^+$  is the light-cone momentum fraction of the initial nucleon carried by the interacting pion. In the infinite momentum frame this coincides with the longitudinal momentum fraction, while in the rest frame of the target nucleon, which we will use in the following,  $z$  is expressed as  $z = (k_0 + |\mathbf{k}| \cos \theta)/M$ , where  $M$  is the mass of the nucleon,  $k_0 = M - \sqrt{M^2 + \mathbf{k}^2}$  is the pion energy, and  $\theta$  is the angle between the vector  $\mathbf{k}$  and the  $z$ -axis (which is equal to the angle between the recoil proton momentum  $\mathbf{p}'$  and the photon direction). For ease of notation, we also suppress the explicit dependence of the structure functions on the scale  $Q^2$ .

The function  $f_{\pi N}(z)$  gives the light-cone momentum distribution of pions in the nucleon,

$$f_{\pi N}(z) = c_I \frac{g_{\pi NN}^2}{16\pi^2} \int_0^\infty \frac{dk_\perp^2}{(1-z)z} \frac{G_{\pi N}^2}{(M^2 - s_{\pi N})^2} \left( \frac{k_\perp^2 + z^2 M^2}{1-z} \right), \quad (7)$$

where  $k_\perp$  is the transverse momentum of the pion,  $g_{\pi NN}$  is the  $\pi NN$  coupling constant, and the isospin factor  $c_I = 1$  for  $\pi^0$  ( $p \rightarrow p\pi^0$  or  $n \rightarrow n\pi^0$ ) and  $c_I = 2$  for  $\pi^\pm$  ( $p \rightarrow n\pi^+$  or  $n \rightarrow p\pi^-$ ). The function  $G_{\pi N}$  parametrizes the momentum dependence of the  $\pi NN$  vertex function, which, due to the finite size of the nucleon, suppresses contributions from large- $|\mathbf{k}|$  configurations. Similar expressions (though somewhat more involved) can be written for other contributions, such as from  $\rho$  mesons or with  $\Delta$  baryons in an intermediate state. However, because of the small mass of the pion, the  $\pi N$  configuration is expected to be the dominant one. In Eq. (7) the variable  $s_{\pi N} = (k_\perp^2 + m_\pi^2)/z + (k_\perp^2 + M^2)/(1-z)$

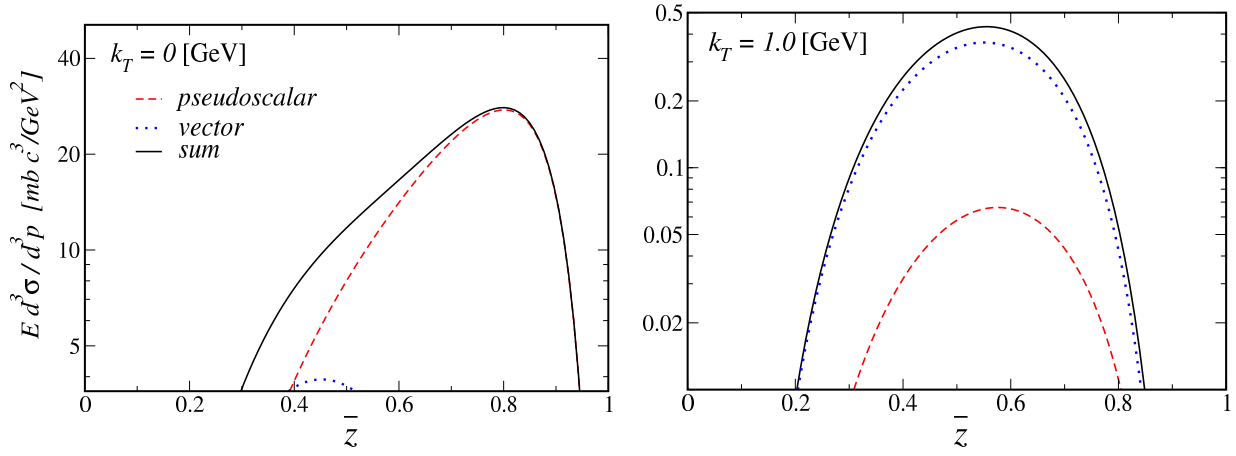


Figure 3: Typical spectra for the differential cross section  $Ed^3\sigma/d^3p'$  in the  $pp \rightarrow nX$  reaction for transverse momentum  $k_\perp = 0$  (left panel) and  $k_\perp = 1$  GeV (right panel), as a function of the light-cone momentum fraction  $\bar{z} \equiv 1 - z$ . The pseudoscalar  $\pi$  (red dashed lines) and vector  $\rho$  (blue dotted lines) contributions, and their sum (black solid lines), are indicated explicitly.

represents the total squared center of mass energy of the intermediate  $\pi N$  system, and is related to the pion virtuality  $t$  by  $t - m_\pi^2 = z(M^2 - s_{\pi N})$ .

The form factor  $G_{\pi N}$  (or more generally  $G_{MN}$  for a meson  $M$ ) can be constrained by comparing the meson cloud contributions with data on inclusive  $pp \rightarrow nX$  scattering, as performed by Holtmann *et al.* [15]. For the purpose of this proposal, we use the parametric form

$$G_{\pi N} = \exp \left[ (M^2 - s_{\pi N})/\Lambda^2 \right], \quad (8)$$

where  $\Lambda$  is the form factor cutoff parameter. (Note that in Ref. [15] a parametrization of the form  $\exp[(M^2 - s_{\pi N})/2\Lambda^2]$  is used, so that the corresponding cutoffs there are smaller by a factor of  $\sqrt{2}$ .) An illustration of the typical spectra for the differential cross section  $Ed^3\sigma/d^3p'$  in the  $pp \rightarrow nX$  reaction arising from  $\pi$  and  $\rho$  exchange is shown in Fig. 3 as a function of the light-cone momentum fraction  $\bar{z} \equiv 1 - z$  carried by the final nucleon, for two values of the transverse momentum  $k_\perp$ . For small  $k_\perp$  the  $\pi$  exchange contribution clearly dominates the  $\rho$  at all  $\bar{z}$ , while at larger momenta the contributions from heavier mesons such as the  $\rho$  become more important.

Using the cutoff parameters constrained by the inclusive hadronic  $pp \rightarrow nX$  data, which were found in Ref. [15] to be  $\Lambda_{\pi N} = \Lambda_{\rho N} = 1.56 \pm 0.07$  GeV and  $\Lambda_{\pi \Delta} = \Lambda_{\rho \Delta} = 1.39 \pm 0.07$  GeV, the light-cone momentum distributions  $f(z)$  are shown in Fig. 4. The principal model uncertainty in these results comes from the ultraviolet regulator  $G$  used to truncate the  $k_\perp$  integrations in the distribution functions. Various functional forms have been advocated in the literature aside from the  $s$ -dependent exponential form factor in Eq. (8), and we compare several of these, including  $s$ - and  $t$ -dependent dipole forms, in Fig. 5. For the  $s$ - and  $t$ -dependent forms in particular, the differences are noticeable mostly at small values of  $z$ , where the  $t$ -dependent parametrization (of the form  $G \sim 1/(t - \Lambda^2)^2$ ) tends to give somewhat larger distributions that are peaked at smaller  $z$ , compared with the  $s$ -dependent form, which tend to be broader.

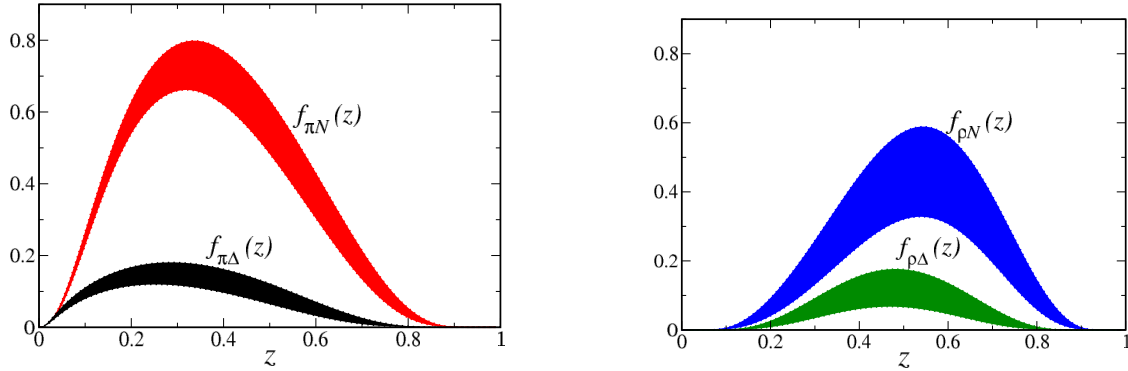


Figure 4: Light-cone momentum distributions of the pion,  $f_{\pi N}$  and  $f_{\pi\Delta}$  (left panel) and the  $\rho$  meson,  $f_{\rho N}$  and  $f_{\rho\Delta}$  (right panel), as a function of the meson light-cone momentum fraction  $z$ . The error bands correspond to the cutoff parameter ranges as given in the text.

Convoluting the light-cone distributions with the structure function of the meson as in Eq. (6), the resulting contributions from the  $\pi N$  and  $\rho N$  intermediate states to the inclusive  $F_2$  structure function of the proton is illustrated in Fig. 6. For the meson structure function we use the parametrization from GRV, and assume that  $F_{2\pi}(x) \approx F_{2\rho}(x)$ . The results are plotted for fixed values of the scattering angle of the final state electron  $\theta_e$ , which determines the  $Q^2$  dependence of the contribution at a given  $x$ . For angles between  $\theta_e = 15^\circ$  and  $40^\circ$  the  $Q^2$  dependence is rather negligible due to the mild  $Q^2$  dependence of the meson structure function. For the fully integrated results of Fig. 6, the model uncertainties are greatest for the lowest accessible values to the proposed experiment of  $x \sim 0.05$ .

### 1.2.2 Tagged Structure Functions

While the inclusive reactions require integration of the pion momentum over all possible values, detecting the recoil proton in the final state allows one to dissect the internal structure with significantly more detail and increase the sensitivity to the dynamics of the meson exchange reaction. In general, we will be interested in the relative contributions of the semi-inclusive reaction with respect to the inclusive process, the ratio of these two being a measurement of the fracture function. In practice, the semi-inclusive structure function will be given by the unintegrated product

$$F_2^{(\pi N)}(x, z, k_\perp) = f_{\pi N}(z, k_\perp) F_{2\pi}\left(\frac{x}{z}\right), \quad (9)$$

where the unintegrated distribution function  $f_{\pi N}(z, k_\perp)$  is defined by

$$f_{\pi N}(z) = \frac{1}{M^2} \int_0^\infty dk_\perp^2 f_{\pi N}(z, k_\perp^2). \quad (10)$$

The dependence of the tagged structure functions on the kinematical variables that are measured experimentally can be studied by relating the magnitude of the 3-momentum

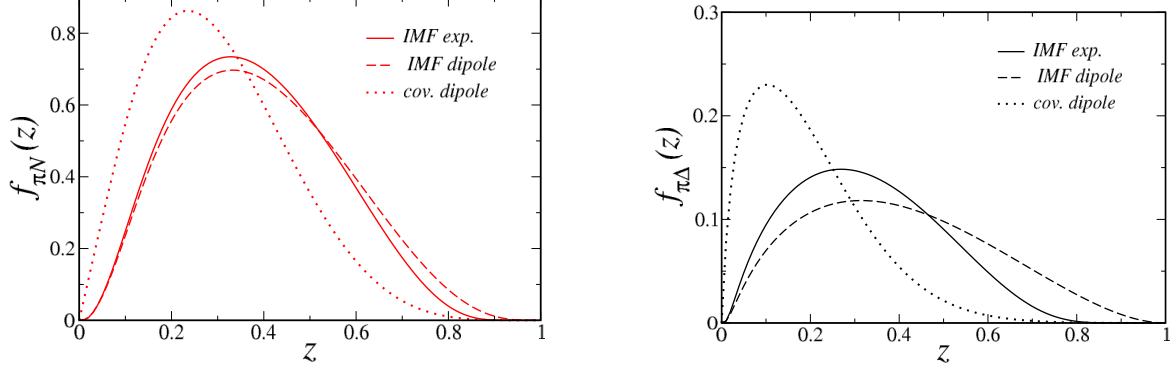


Figure 5: Light-cone momentum distributions for the  $\pi N$  (left panel) and  $\pi\Delta$  (right panel) intermediate states, for several different functional forms of the form factor  $G$  in Eq. (7): “IMF” refers to  $s$ -dependent forms such as in Eq. (8), while “cov” denotes a form factor that depends only on the variable  $t$ .

$\mathbf{k}$  of the exchanged pion in the target rest frame to the pion’s transverse momentum  $k_\perp$  and light-cone fraction  $z$ ,

$$\mathbf{k}^2 = k_\perp^2 + \frac{[k_\perp^2 + (1 - [1 - z]^2)M^2]^2}{4M^2(1 - z)^2}. \quad (11)$$

Experimentally, the quantities most readily measured are the momentum of the produced proton,  $\mathbf{p}'$ , which in the rest frame is  $\mathbf{p}' = -\mathbf{k}$ , and the scattering angle  $\theta_{p'} = \theta$  of the proton with respect to the virtual photon direction. In the limit  $k_\perp^2 = 0$ , the magnitude of  $\mathbf{k}$  becomes

$$|\mathbf{k}|_{k_\perp=0} = \frac{zM}{2} \left( \frac{2 - z}{1 - z} \right), \quad (12)$$

which imposes the restriction  $z \lesssim |\mathbf{k}|/M$ . This relation is illustrated in Fig. 7 for values of  $z$  up to 0.2.

This is a critical guiding parameter for the proposed experiment. Since we seek to measure the low momentum region where pseudo scalar production dominates, the region of interest becomes  $z \lesssim 0.2$ . This corresponds to the measurable proton range,  $60 \lesssim \mathbf{k} \lesssim 400$  MeV/c, of the radial time projection chamber discussed in detail below. It is important to note that, since  $x < z$ , this also determines both the  $x$  and  $Q^2$  (given the maximum beam energy) of the experiment.

The kinematic restrictions on  $|\mathbf{k}|$  for a given  $z$  can also be illustrated by considering the unintegrated light-cone distribution functions as a function of the variable  $t$ . This is relevant since one way of identifying the pion exchange mechanism is through its characteristic  $t$  dependence, which is pronounced near the pion pole at  $t = +m_\pi^2$ . The production of a physical proton (or  $\Delta$  baryon) in the final state restricts the maximum value of  $t$ , however (corresponding to the minimum transverse momentum,  $k_\perp = 0$ ), to

$$t_{\min}^N = -\frac{M^2 z^2}{1 - z}, \quad t_{\min}^\Delta = -\frac{(M_\Delta^2 - (1 - z)M^2)z}{1 - z}, \quad (13)$$

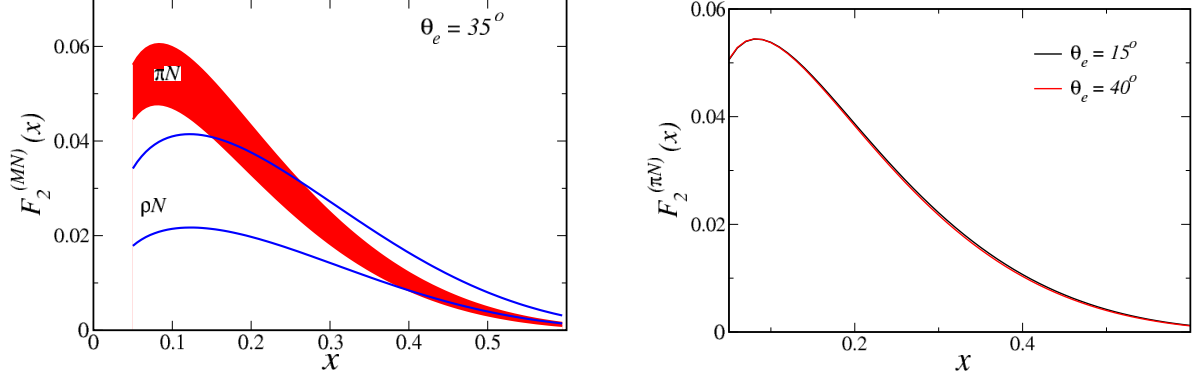


Figure 6: Contributions from  $\pi N$  and  $\rho N$  intermediate states to the inclusive  $F_2$  structure function of the proton for fixed electron scattering angle  $\theta_e = 35^\circ$  (left panel), and at two different angles,  $\theta_e = 15^\circ$  and  $40^\circ$  (right panel) for the  $\pi N$  contributions.

for nucleon  $N$  and  $\Delta$  final states, respectively. Implementing these limits, the  $t$ -dependence of the distributions for  $\pi$  exchange with a nucleon or  $\Delta$  recoil is illustrated in Fig. 8. Note that at the larger  $z$  value there is a considerable gap between the values of  $t$  at which  $\Delta$  production is possible compared with  $N$  production.

Experimentally, the semi-inclusive cross sections will be measured in specific bins of recoil proton momentum  $|\mathbf{p}'| = |\mathbf{k}|$  and scattering angle  $\theta_{p'}$  (or equivalently  $z$  and  $k_\perp$ ). We therefore define the partially integrated semi-inclusive structure function  $F_2^{(\pi N)}(x, \Delta z, \Delta k_\perp^2)$ ,

$$F_2^{(\pi N)}(x, \Delta z, \Delta k_\perp^2) = \frac{1}{M^2} \int_{\Delta z} \int_{\Delta k_\perp^2} f_{\pi N}(z, k_\perp) F_{2\pi}\left(\frac{x}{z}\right), \quad (14)$$

integrated over the range  $\Delta z = [z_{\min}, z_{\max}]$  and  $\Delta k_\perp^2 = [k_{\perp \min}^2, k_{\perp \max}^2]$ . Alternatively, one can define an analogous semi-inclusive structure function integrated over other variables, such as  $|\mathbf{k}|$  and  $\theta_{p'}$ , by  $F_2^{(\pi N)}(x, \Delta|\mathbf{k}|, \Delta\theta_{p'})$ . The proposed experiment will probe the ranges of kinematics  $0.05 \lesssim z \lesssim 0.2$  and  $60 \lesssim |\mathbf{k}| \lesssim 400$  MeV, and angles  $30 \lesssim \theta_{p'} \lesssim 160^\circ$ , with  $x$  in the vicinity of  $x \sim 0.05 - 0.2$ .

Fig. 9 shows the semi-inclusive structure functions  $F_2^{(MN)}(|\mathbf{k}|; \Delta x, \Delta\theta_{p'})$  for  $p \rightarrow \pi^0 p$  and  $p \rightarrow \rho^0 p$ , as a function of the momentum  $|\mathbf{k}|$ , integrated over  $x$  between 0 and 0.6, and over all angles  $\theta_{p'}$  from 0 to  $\pi$ . The structure functions rise with increasing  $|\mathbf{k}|$  in the experimentally accessible region  $|\mathbf{k}| \lesssim 0.5$  GeV, where the  $\rho$  contribution is clearly suppressed relative to the pion contribution. At larger momenta the effects of the meson-nucleon form factors become more important, which suppress the contributions from high- $|\mathbf{k}|$  tails of the distributions. The peak in the  $\pi$  distribution occurs at  $|\mathbf{k}| \approx 0.6$  GeV, while the  $\rho$  distribution peaks at higher momenta,  $|\mathbf{k}| \approx 1.2$  GeV, and has a slower fall-off with  $|\mathbf{k}|$ .

To further illustrate the capability for an experiment at the proposed kinematics to minimize effects from the  $p \rightarrow \rho p$  process, Fig. 10 gives the  $x$  dependence of the semi-inclusive structure function  $F_2^{(MN)}(x, \Delta|\mathbf{k}|, \Delta\theta_{p'})$  for  $p \rightarrow \pi^0 p$  and  $p \rightarrow \rho^0 p$ , integrated



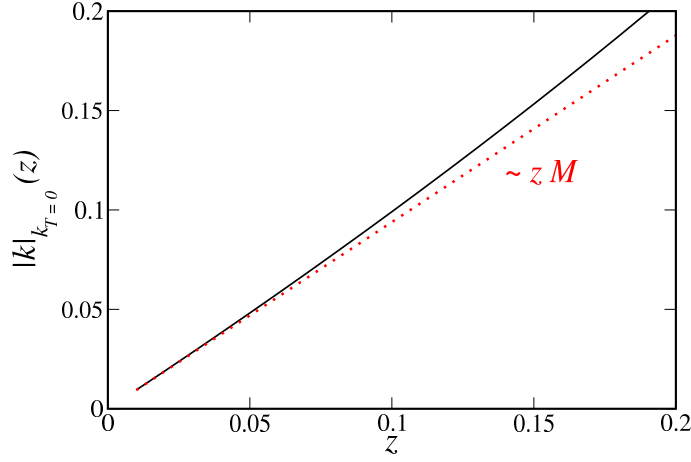


Figure 7: Pion momentum  $|\mathbf{k}|$  as a function of the light-cone fraction  $z$  for  $k_{\perp} = 0$  (black solid). The linear approximation  $\sim zM$  (red dotted) is shown for comparison.

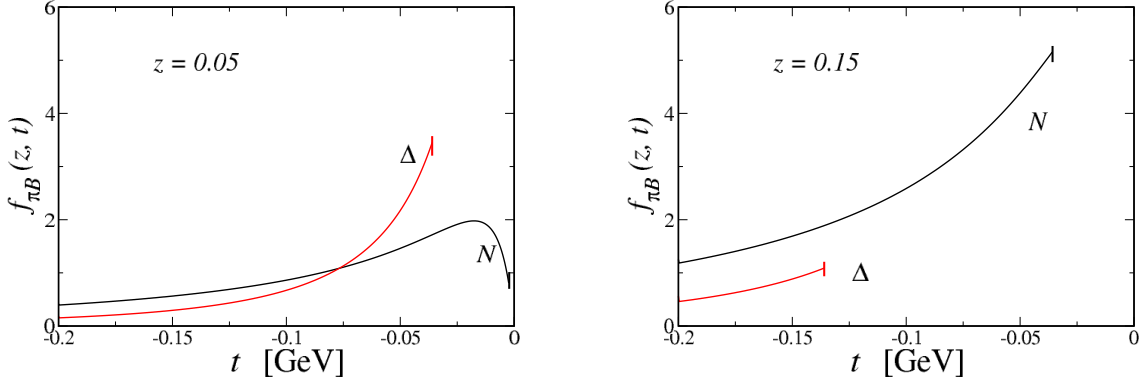


Figure 8: Unintegrated light-cone distribution functions for  $\pi N$  (black solid) and  $\pi\Delta$  (red solid) states as a function of  $t$ , for fixed values of  $z = 0.05$  (left) and  $z = 0.15$  (right).

over the momentum range of this experiment for all angles  $\theta_{p'}$ . The  $\rho$  channel is nearly two orders of magnitude smaller.

The angular dependence of  $F_2^{(MN)}$  as shown in Fig. 11 again shows the dominance of the  $\pi$  over the  $\rho$ . The angular dependence will, moreover, prove to be important to removing the experimental background arising from low energy  $e-p$  scattering. Elastically scattered protons in a comparable energy range to the TDIS recoil protons are essentially confined around  $90^\circ$ , allowing for a separation between these and the TDIS recoil protons of interest.

The effect of the pion-nucleon form factors are illustrated in Fig. 12, where the semi-inclusive structure functions are shown as a function of  $x$ , integrated over the momentum range  $\Delta|\mathbf{k}| = [60, 250]$  MeV. The results with the  $s$ -dependent (IMF) exponential and dipole form factors are compared with the  $t$ -dependent dipole form factor, as well as with the calculation without any form factor suppression of the ultraviolet contributions. As

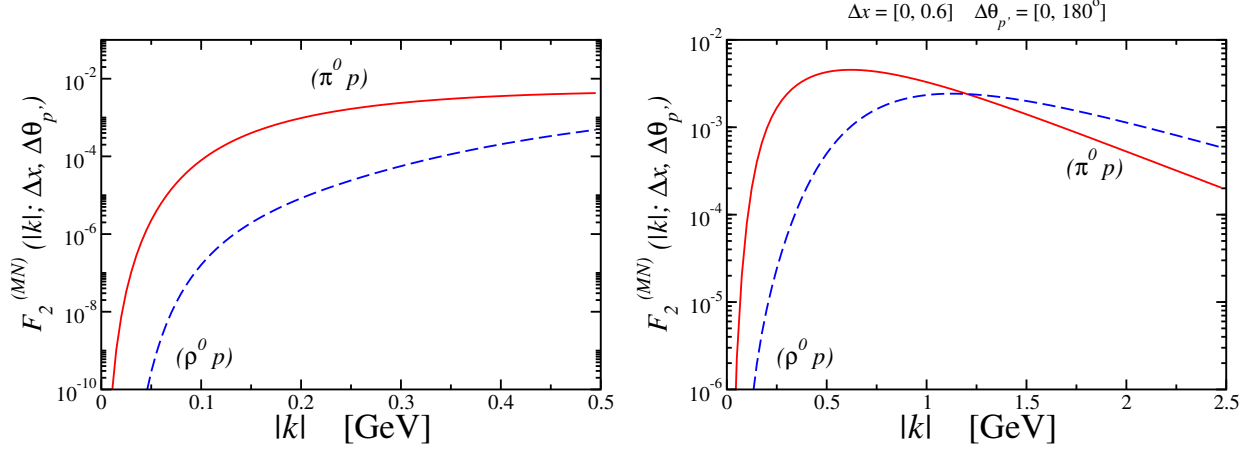


Figure 9: Semi-inclusive structure functions  $F_2^{(MN)}(|\mathbf{k}|; \Delta x, \Delta\theta_{p'})$  for the  $p \rightarrow M p$  process, with  $M = \pi^0$  (red solid) and  $M = \rho^0$  (blue dashed), as a function of the recoil proton momentum  $|\mathbf{k}|$ , integrated over  $\Delta x = [0, 0.6]$  and all angles  $\theta_{p'}$ . The left panel shows the function over the experimentally accessible range for  $|\mathbf{k}|$  up to 0.5 GeV, while the right panel shows the extended range up to  $|\mathbf{k}| = 2.5$  GeV.

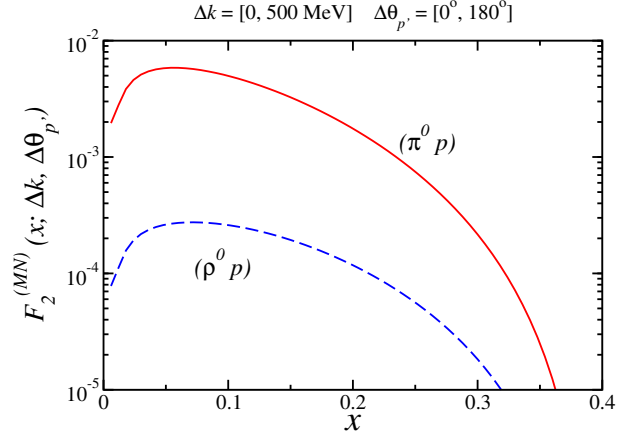


Figure 10:  $x$  dependence of the semi-inclusive structure function  $F_2^{(MN)}(x, \Delta|\mathbf{k}|, \Delta\theta_{p'})$  for  $p \rightarrow \pi^0 p$  (red solid) and  $p \rightarrow \rho^0 p$  (blue dashed), integrated over the momentum range  $\Delta|\mathbf{k}| = [0, 500]$  MeV and over all angles  $\theta_{p'}$ .

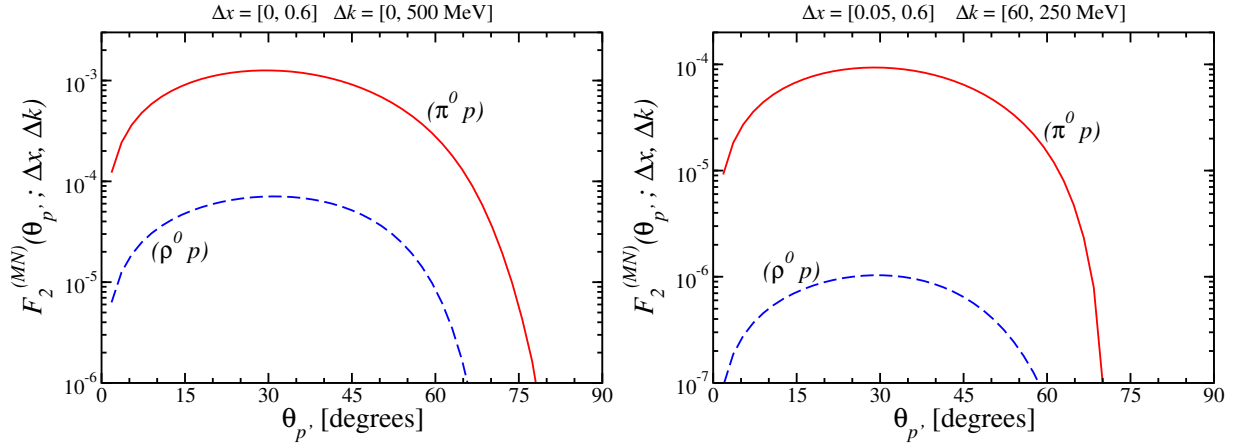


Figure 11:  $\theta_{p'}$  dependence of the tagged structure function  $F_2^{(\pi p)}(\theta_{p'}, \Delta x, \Delta|\mathbf{k}|)$  for neutral exchange in  $p \rightarrow \pi^0 p$  (red, solid) and  $p \rightarrow \rho^0 p$  (blue, dashed). The left panel plots the more inclusive integration ranges  $\Delta x = [0, 0.6]$  and  $\Delta|\mathbf{k}| = [0, 500]$  MeV, whereas the right panel show the same, but for the more constrained integration ranges  $\Delta x = [0.05, 0.6]$  and  $\Delta|\mathbf{k}| = [60, 250]$  MeV, appropriate for the proposed measurement.

expected, the form factor dependence is relatively mild in this momentum interval, and it is only for larger momenta ( $|\mathbf{k}| \gtrsim 0.5$  GeV) that the form factor model becomes significant.

The dependence of the semi-inclusive structure function  $F_2^{(\pi N)}(x, \Delta|\mathbf{k}|, \Delta\theta_{p'})$  on the pion structure function parametrization are shown in Fig. 13 as a function of  $x$ , integrated over the momentum range  $\Delta|\mathbf{k}| = [60, 250]$  MeV and angular range  $\Delta\theta_{p'} = [30^\circ, 180^\circ]$  of the proposed experiment. The results with the GRV parametrization [23] of the pion parton distribution functions are compared with those using the MRS parametrization [24] with different amounts of sea, ranging from 10% to 20%. The pion structure function parameterizations are all similarly constrained by the pion–nucleon Drell-Yan data at Fermilab at intermediate and large values of  $x$ . The variation in the computed semi-inclusive proton structure function from uncertainties in the pion distribution functions is therefore smaller than the uncertainties from the pion–nucleon vertex form factor dependence.

Fig. 14 depicts, finally, the  $x$  dependence of the inclusive structure function  $F_{2p}(x)$  for the proton, for comparison to both the structure function for the full pionic content of the proton  $F_2^{\pi p}(x)$  as well as to the tagged, semi-inclusive structure function  $F_2^{(\pi p)}(x, \Delta|\mathbf{k}|, \Delta\theta_{p'})$ , for the indicated ranges in tagged, recoil proton momentum. The lowest momentum protons will be measured within the spectrometer acceptance, but clearly with lower statistics. Each momentum range corresponds by definition to a range in  $t$ , causing these low momentum protons to be of particular interest for extrapolation very close to the pion pole. It is planned that a range of  $t$  (proton momentum) points will be obtained at multiple values of  $x$  to map out this dependence. The full range of expected data are shown on this plot, as is an example plot for the  $t$  extrapolation, in the Results section of this proposal.

Fig. 15 shows the same structure function quantities for the neutron as were just shown for the proton, but here with a comparison instead to the strength of other physics channels, the tagged structure functions for  $(\pi^- p)$ ,  $(\rho^- p)$ , and  $(\pi^0 \Delta^0 + \pi^- \Delta^+)$ , rather than to

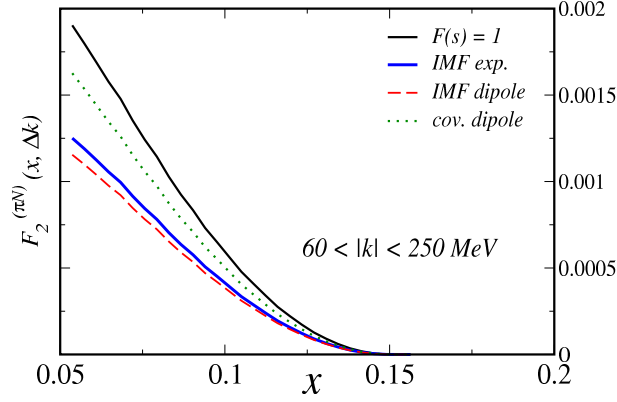


Figure 12: Semi-inclusive structure function  $F_2^{(\pi N)}(x; \Delta|\mathbf{k}|, \Delta\theta_{p'})$  as a function of  $x$ , integrated over the momentum range  $\Delta|\mathbf{k}| = [60, 250]$  MeV and accessible angles  $\Delta\theta_{p'}$ . The results with the  $s$ -dependent (IMF) exponential (blue solid) and dipole (red dashed) form factors are compared with the  $t$ -dependent (covariant) dipole form factor (green dotted), and with no form factor (black solid).

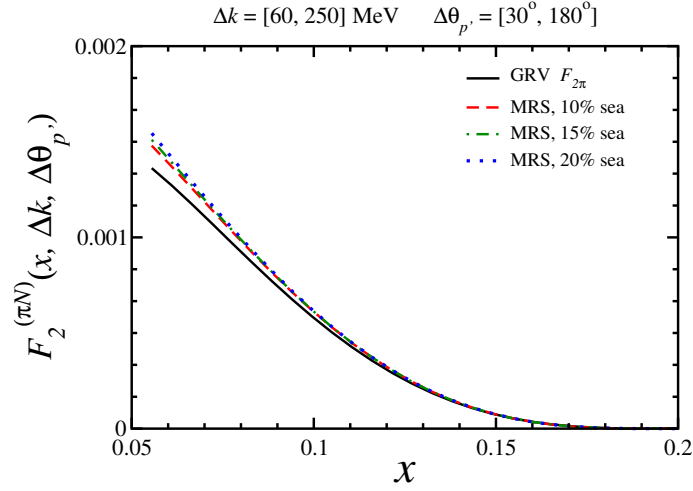


Figure 13: Semi-inclusive structure function  $F_2^{(\pi N)}(x, \Delta|\mathbf{k}|, \Delta\theta_{p'})$  for the  $p \rightarrow \pi^0 p$  process, integrated over the momentum range  $\Delta|\mathbf{k}| = [60, 250]$  MeV and angular range  $\Delta\theta_{p'} = [30^\circ, 180^\circ]$ . The results with the GRV [23] (black solid) parametrization of the pion structure function are compared with those using the MRS [24] fit with different amounts of sea, 10% (red dashed), 15% (green dot-dashed) and 20% (blue dotted).

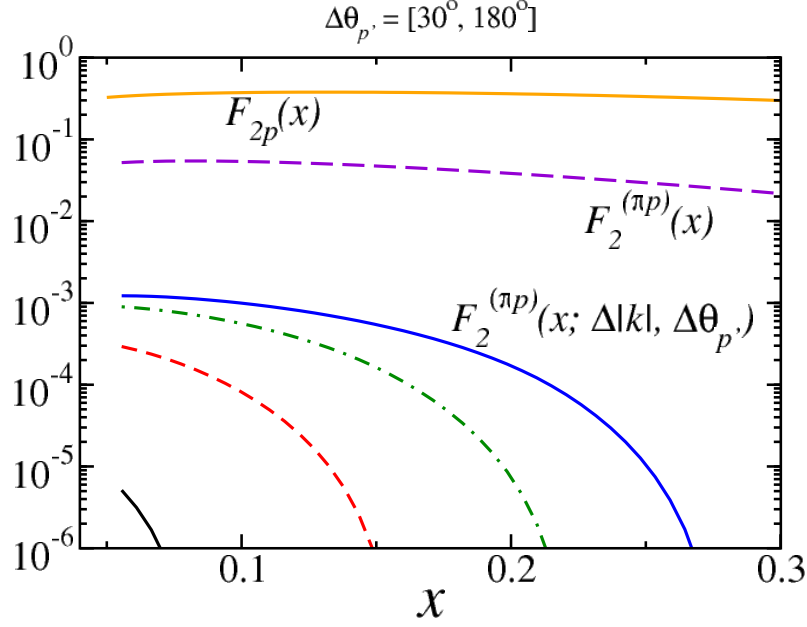


Figure 14:  $x$  dependence of the semi-inclusive structure function  $F_2^{(\pi p)}(x, \Delta|\mathbf{k}|, \Delta\theta_{p'})$  (blue curve). For comparison, the total integrated  $\pi p$  contribution  $F_2^{(\pi p)}$  to the inclusive proton structure function is shown (violet dashed), as is the total inclusive  $F_{2p}$  structure function (orange solid). The lower bands follow from varying the integration range  $\Delta|\mathbf{k}|$ ; they correspond to  $\Delta|\mathbf{k}| = [60, 100]$  MeV (black, solid),  $\Delta|\mathbf{k}| = [100, 200]$  MeV (red, dashed),  $\Delta|\mathbf{k}| = [200, 300]$  MeV (green, dot-dashed), and  $\Delta|\mathbf{k}| = [300, 400]$  MeV (blue, solid).

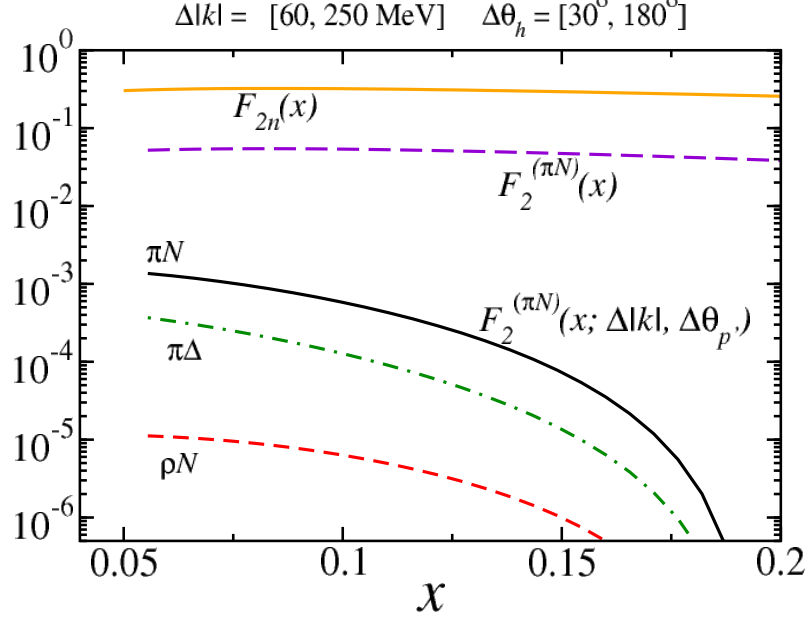


Figure 15: Structure functions as in Fig. 14, but now for the  $x$  dependence of  $F_2^{(\pi p)}(x, \Delta|\mathbf{k}|, \Delta\theta_{p'})$  for charge-exchange in, e.g., the  $n \rightarrow \pi^- p$  process. The tagged semi-inclusive structure function for  $(\pi^- p)$  (black, solid),  $(\rho^- p)$  (red, dashed), and  $(\pi^0 \Delta^0 + \pi^- \Delta^+)$  (green, dot-dashed) are compared with the inclusive structure function of the neutron  $F_{2n}(x)$  (orange), and the fully-integrated  $(\pi^- p)$  contribution  $F_2^{\pi N}(x)$  (violet, dashed).

the measured momentum range components. The neutron target is planned to be tagged by two protons in coincidence with the scattered electron, one as was utilized successfully at backward angles in BONUS to identify the nearly free neutron in deuterium, and the other the recoil, tagged, semi-inclusive proton at more forward angles as has been here discussed. The  $\rho$  component of this process is nearly negligible in comparison to the  $\pi$ , and the already small intermediate  $\Delta$  resonance component to the process may be further reduced by a kinematic cut discussed later leveraging the differences in  $t_{min}$  as in Fig. 8. The momentum ranges as in Fig. 14 would appear nearly the same here for the neutron as they do for the proton and, conversely the other channels depicted here for the neutron would appear quite similarly for the proton. As with the proton, the full range of expected data are shown on this plot in the Results section of this proposal.

### 1.3 Measurement of the Pion Structure Function via the Sullivan Process

The pion, being the lightest and simplest hadron, has a central role in our current description of nucleon and nuclear structure. The pion has been used to explain the long-range nucleon-nucleon interaction and also to explain the flavor asymmetry of the quark sea in the nucleon. Moreover, the masses of light mesons such as the pion are believed to arise from dynamical chiral symmetry breaking [45], and thus models of the pion must account for both its role as the Goldstone boson of quantum chromodynamics (QCD) and as a quark-antiquark system.

Experimental knowledge of the partonic structure of the pion is very limited due to the lack of a stable pion target. Most of the current knowledge of the pion structure function in the valence region is obtained primarily from pionic Drell-Yan scattering [46]-[48], and in the pion sea region at low Bjorken- $x$ , from hard diffractive processes measured on  $e-p$  collisions at HERA [49]. The existing data on the pion structure function from Drell-Yan scattering is shown in Fig 16. Also shown, in Fig. 17, are the pion structure function at low  $x$  deduced from hard diffractive process, where forward-going neutrons or protons were tagged in coincidence with the DIS events. These results seem to indicate that the pion sea has approximately one-third of the magnitude of the proton sea, while from the parton model one expects the pion sea to be two-thirds of the proton sea.

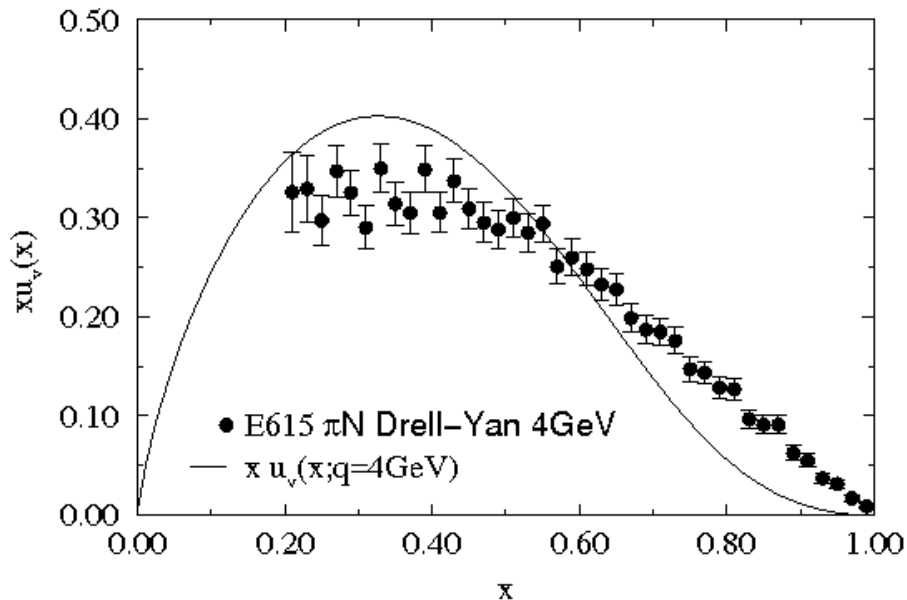


Figure 16: Existing data for the pion structure function from Drell-Yan Experiment E615 [46]. The solid curve is the calculation from Ref. [53].

There are several theoretical calculations of the pion structure in the valence region, however, they tend to disagree with each other. The parton model [50], perturbative QCD based models [51, 52] and some non-perturbative models such as those based on the Dyson-Schwinger Equation [53]-[56] predict a  $(1-x)^a$  dependence with  $a \geq 2$ . On the other hand

relativistic constituent quark models [57, 58], Nambu-Jona-Lasinio models [59]-[62], the Drell-Yan-West relation [63, 64] and even arguments based on quark-hadron duality [65] favor a linear  $(1 - x)$  dependence of the pion structure function at high- $x$ . Calculations of the pion structure function in the pion sea region, such as those of the chiral quark model [66], also disagree with the extraction from the HERA data, in fact these models predict that the momentum fraction of pion sea is larger than the proton sea. These discrepancies tell us that it is essential to measure the pion structure function over a wide range of  $x$  using new techniques.

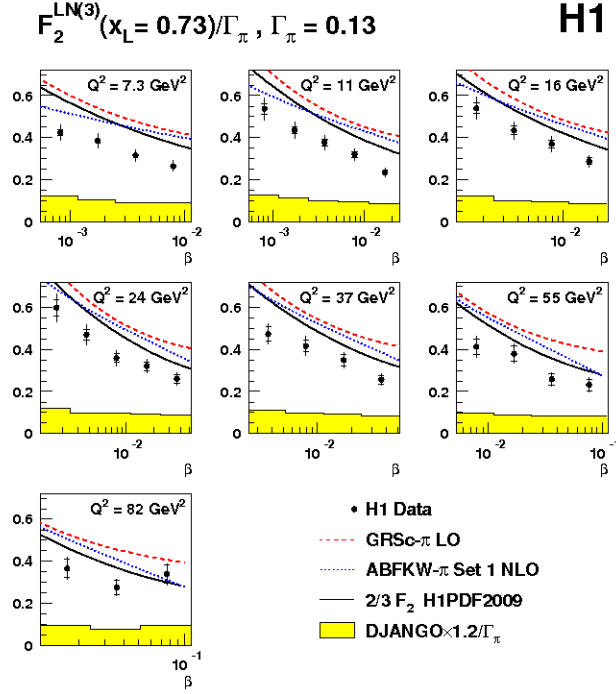


Figure 17: Pion structure functions measured by H1 [49] in comparison with parameterizations of various pion parton distribution functions. The Bjorken- $x$  of the pion is denoted as  $\beta$ .

One such technique is to measure the contribution to the electron Deep Inelastic Scattering (DIS) off the meson cloud of a proton target, as pointed out by Sullivan [67] (Fig. 18). This so-called Sullivan process was shown to persist even at large  $Q^2$  scales. An immediate consequence of the Sullivan process is that the nucleon parton distributions contain a component which can be attributed to the meson cloud. This intriguing idea remained untested for many years. In the early 1980s, Thomas [68] predicted several implications of the Sullivan process for nucleon parton distributions using a cloudy-bag model for describing the meson cloud. In particular, it was predicted that the nucleon sea should have an up/down sea-quark flavor asymmetry, as well as an  $s/\bar{s}$  asymmetry for the strange quark sea. The earliest parton models assumed that the proton sea was flavor symmetric, even though the valence quark distributions are clearly flavor asymmetric. The assumption of flavor symmetry was not based on any known physics, and it remained



to be tested by experiments. A direct method to check this assumption is to compare the sea in the neutron to that in the proton by measuring the Gottfried integral in DIS. The Gottfried Sum Rule (GSR) gives the following relation for the proton and neutron structure functions  $F_2^p$  and  $F_2^n$ :

$$I_{\text{GSR}} = \int_0^1 [F_2^p(x) - F_2^n(x)]/x dx = \frac{1}{3} + \frac{2}{3} \int_0^1 [\bar{u}(x) - \bar{d}(x)] dx = \frac{1}{3}. \quad (15)$$

In the early 1990s, the NMC collaboration reported[69] an observation of the violation of the GSR[70],  $I_{\text{GSR}} = 0.235 \pm 0.026$ . Since the GSR is derived under the assumption of  $\bar{d}(x) = \bar{u}(x)$ , the NMC result strongly suggests that this assumption is invalid. Indeed, Eq.1 and the NMC result imply that

$$\int_0^1 (\bar{d}(x) - \bar{u}(x)) dx = 0.148 \pm 0.039 \quad (16)$$

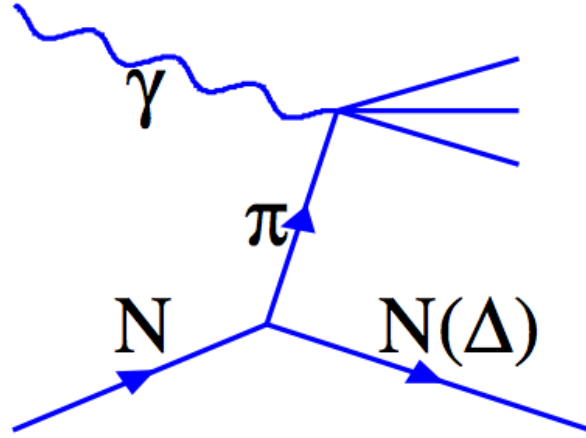


Figure 18: The Sullivan process.

Independent confirmation of the  $\bar{d}/\bar{u}$  flavor asymmetry were later provided by Drell-Yan experiments [71, 72, 73, 74] and the semi-inclusive DIS experiment [75]. Figure 19 shows the E866 result on  $\bar{d}(x) - \bar{u}(x)$  at  $Q^2 = 54 \text{ GeV}^2/c^2$ . The surprisingly large asymmetry between  $\bar{d}$  and  $\bar{u}$  is observed over a broad range of  $x$ . The E866 data provide a direct evaluation of the  $d - u$  integral, namely,  $\int_0^1 (\bar{d}(x) - \bar{u}(x)) dx = 0.118 \pm 0.012$ , which is in good agreement with the NMC result shown in Eq. 2. The observation of  $\bar{u}$ ,  $\bar{d}$  flavor asymmetry has inspired many theoretical work regarding the origin of this asymmetry. Perturbative QCD, in which  $q\bar{q}$  sea is generated from the  $g \rightarrow q\bar{q}$  splitting, has difficulties explaining such an asymmetry. The small  $d, u$  mass difference (actually,  $m_d > m_u$ ) of 2 to 4 MeV compared to the nucleon confinement scale of 200 MeV does not permit any appreciable difference in their relative production by gluons.

At any rate, one observes a surplus of  $\bar{d}$  which is the heavier of the two species. Field and Feynman long time ago speculated that the  $g \rightarrow u\bar{u}$  process would be suppressed relative to  $g \rightarrow d\bar{d}$  due to Pauli-blocking effect and the presence of two  $u$ -quarks as compared

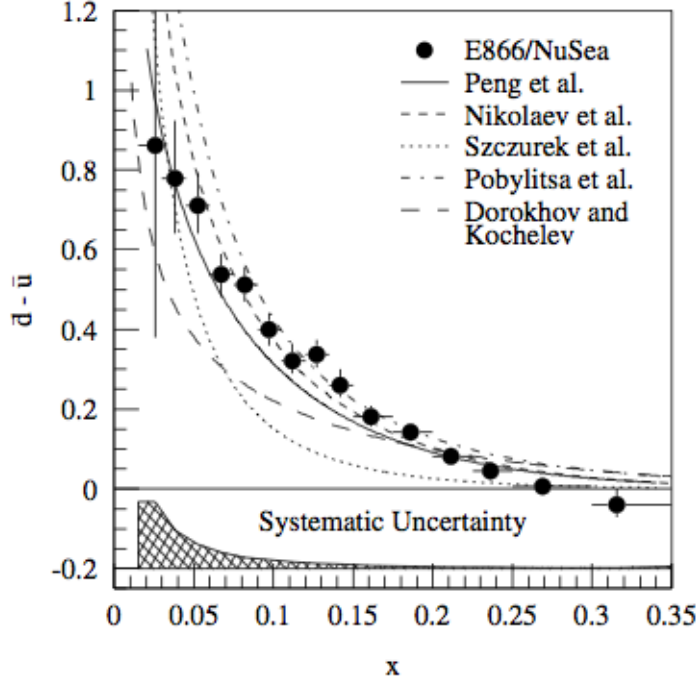


Figure 19: Comparison of the E866  $\bar{d}\bar{u}$  data with various model calculations [74]

to a single  $d$ -quark in proton. Steffen and Thomas have examined the consequences of Pauli-blocking, concluding that the effect of blocking is small [76]. Thus, another, presumably non-perturbative, mechanism must account for the large measured  $\bar{d}$ ,  $\bar{u}$  asymmetry. Many of the non-perturbative approaches to explain the  $\bar{d}$ ,  $\bar{u}$  asymmetry involve the use of isovector meson (particularly pion). Recent reviews [77, 78, 79] have extensive discussions on various theoretical models. In the meson-cloud model, the virtual pion is emitted by the proton and the intermediate state is pion + baryon. More specifically, the proton is taken to be a linear combination of a “bare” proton plus pion-nucleon and pion-delta states, as below,

$$\begin{aligned}
 |p\rangle \rightarrow & \sqrt{1-a-b}|p_0\rangle + \sqrt{a}\left(-\sqrt{\frac{1}{3}}|p_0\pi^0\rangle + \sqrt{\frac{2}{3}}|n_0\pi^+\rangle\right) \\
 & + \sqrt{b}\left(\sqrt{\frac{1}{2}}|\Delta_0^+\pi^-\rangle - \sqrt{\frac{1}{3}}|\Delta_0^+\pi^0\rangle + \sqrt{\frac{1}{6}}|\Delta_0^0\pi^+\rangle\right)
 \end{aligned} \tag{17}$$

The subscript zeros on the virtual baryon states indicate that they are assumed to have symmetric seas, so the asymmetry in the antiquarks must be generated from the pion valence distribution. The coefficients  $a$  and  $b$  are the fractions of the  $\pi N$  and  $\pi\Delta$  configurations, respectively, in the proton. These fractions can be calculated using the  $\pi NN$  and  $\pi N\Delta$  couplings, and form factors as taken from experiment. The asymmetry in the proton sea arises because of the dominance of  $\pi^+$  among the virtual configurations. Figure 19 shows that the pion-cloud model can reproduce the  $x$ -dependence of the  $\bar{d}\bar{u}$  distribution very well. The success of the meson-cloud model in explaining the  $\bar{d}$ ,  $\bar{u}$  asymmetry sug-

gests that a direct measurement of the meson cloud in DIS should be feasible. The idea is that the meson cloud in the nucleon could be considered as a virtual target to be probed by various hard processes including DIS and Drell-Yan.

In summation,

- the partonic structure of the pion, the lightest and simplest hadron is not well measured over the entire Bjorken- $x$  range and the predictions of models describing the pion structure differ significantly. There is a great need to measure the pion structure with a new and independent technique.
- The well established quark flavor asymmetry in the nucleon sea can be explained in terms of the meson cloud model.
- The Sullivan process allows access to the meson cloud of the nucleon. Measurements at JLab would allow a rigorous determination of the pion-cloud content of the nucleon, and test the theoretical models that explain the  $d\bar{u}$ / $u\bar{d}$  asymmetry, observed in the Drell-Yan experiments, in terms of the pion cloud.
- Using the Sullivan process to measure the pion structure function would help establish the mesonic content of the nucleon and also provide a new and independent method to access the partonic structure of the pion.
- The measurement of pion parton distribution using the Drell-Yan process (Fermilab E615 and possibly at COMPASS in the future) is limited to charged pions. At JLab, the measurements can be extended to neutral pion and check the validity of isospin symmetry.

The idea of considering the meson cloud as a virtual pion target was used at the HERA  $e - p$  collider to measure the pion structure functions at low- $x$  in a hard diffractive process, where forward-going neutrons or protons were tagged in coincidence with the DIS events, as shown in Fig. 18. While the HERA experiments have provided very interesting first data on the extraction of pion structure functions using the Sullivan process, there are many reasons for extending such measurements to JLab energies. First, the HERA kinematics is limited to very low  $x$  region, where no independent measurement of pion structure functions exists. This makes it difficult to check the validity of the interpretation of the HERA data in terms of the meson-cloud model. The 12 GeV upgrade of JLab will allow access kinematics of  $|t| < 0.2 \text{ GeV}^2$ ,  $Q^2 > 1 \text{ GeV}^2$  and  $M_x > 1.0 \text{ GeV}/c^2$ , which will enable us to probe the high and intermediate  $x$  region of the pion, where some data on the structure functions already exist from the pion-induced Drell-Yan experiments. A comparison of the  $x$ -dependence of the pion structure function deduced from the Sullivan process and the Drell-Yan process would provide a very stringent test of the pion-cloud model. Second, the large angular and kinematic coverage for the re-coiling proton (or proton pair) detected using the BONUS-12 recoil detector, in coincidence with the scattered electron, would allow a detailed study of the Sullivan process as a function of several variables including the recoiling proton momentum and angles. Third, the electron will be detected in the SBS with the hadron calorimeter replaced with the large angle calorimeter (LAC), or in the BigBite spectrometer. The SBS and recoil detector may allow a

detection of the  $\Lambda \rightarrow p\pi^-$  decay, making a measurement of the  $p \rightarrow K^+\Lambda$  kaon cloud in the nucleon potentially feasible. This could lead to a measurement of kaon structure functions. Finally, the Sullivan process could contribute to the proposed  $d(e, e'p)X$  measurement of the neutron structure function (BONUS-12). It is important to determine experimentally the magnitude of the Sullivan process by detecting both the  $p(e, e'p)X$  and  $d(e, e'pp)X$  reactions. Such measurements would provide crucial inputs needed for an accurate extraction of the neutron structure functions. The charged pion exchange process has the advantage of less background from Pomeron and Reggeon process [80] and the charged pion cloud is double of the neutral pion cloud in the proton.

In this experiment we will measure the semi-inclusive structure function of the leading proton,  $F_2^{LP(4)}$ , which is related to the measured cross-section as;

$$\frac{d^4\sigma(ep \rightarrow e' X p')}{dx dQ^2 dy dt} = \frac{4\pi\alpha^2}{xQ^4} \left(1 - y + \frac{y^2}{2[1 + R]}\right) F_2^{LP(4)}(x, Q^2, y, t), \quad (18)$$

where  $y = P.q/P.l$ ,  $Q^2 = -(l - l')^2$ ,  $x = Q^2/(2P.q)$  and  $t = (P - P')^2$  where  $P(P')$  are the initial(scattered) proton 4 vector,  $q = l - l'$  and  $l(l')$  are the initial (scattered) lepton and  $R$  is the ratio of the cross-section for longitudinally and transversely polarized virtual photons. The measured cross-section can be integrated over the proton momentum (which is effectively an integration over  $t$  [49]) to obtain the leading proton structure function  $F_2^{LP(3)}$ . The pion structure function  $F_2^\pi$  can then be extracted from  $F_2^{LP(3)}$  using models, such as the Regge model of baryon production. In the Regge model the contribution of a specific exchange  $i$  is defined by the product of its flux  $f_i(y, t)$  and its structure function  $F_2^i$  evaluated at  $(x_i, Q^2)$ . Thus,

$$F_2^{LP(3)} = \sum_i \left[ \int_{t_0}^{t_{min}} f_i(z, t) \right] F_2^i(x_i, Q^2), \quad (19)$$

where  $i$  is pion  $\rho$ -meson etc, and the  $t$  corresponds to the range of  $p_T$  analyzed.

The extraction of the pion structure function will have to be corrected for a number of complications to this simple picture, such as the absorptive effect of other mesons. However, these corrections are minimized by measuring at the lowest proton momentum possible from the reaction. This minimizes the absorptive correction since at lower momenta the pion cloud is further from the bare nucleon. In addition, the low proton momentum ensures that the higher meson mass exchanges are suppressed by the energy denominator.

The largest uncertainty in extracting the pion structure function arises from the knowledge of the pion flux in the framework of the pion cloud model. This can be stated, alternatively, as the percentage of the measured fracture function attributable to the pion. One of the main issues is whether to use the  $\pi NN$  form factor or the Reggeized form factor. The difference between these two methods can be as much as 20% [82]. From the N-N data the  $\pi NN$  coupling constant is known to 5% [83]. If we assume that all corrections can be performed with a 50% uncertainty and we assume a 20% uncertainty in the pion flux factor, the overall systematic uncertainty will be 24%. However, by comparing to pionic Drell-Yan data at moderate  $x$  (where it is most reliable), we can have a measurement of the pion flux factor. For example the pion structure function at  $x=0.5$

has been measured from the pionic Drell-Yan data to an accuracy of 5% [46]-[48]. The proposed data will very slightly overlap the Drell-Yan data, allowing us to leverage this precision and likely reduce our projected uncertainty even further.

## 1.4 Impact for the Jefferson Lab 12 GeV Program and Beyond

The remarkably successful application of the quarkparton model in the description of deep-inelastic scattering (DIS) data over a very large kinematic domain has propelled this simple picture of the nucleon at high energies into becoming part of the common language employed by medium and high energy physicists. Massive and numerous global fitting efforts utilize perturbative QCD to extract the universal parton distribution functions from a host of high energy data including from decades of precision DIS experiments. Nevertheless, the QCD-improved parton model cannot, by itself, give a complete description of the structure of the nucleon at high energies. It is unable to (nor was it intended to) explain the spectrum of the nucleons non-perturbative features. Here, effective degrees of freedom, for example in the form of a mesonic cloud of the nucleon, have been evoked to describe the long range structure of the nucleon. This has proved a reasonable approach in explaining for instance the deviation from the QCD-parton model prediction for the Gottfried sum rule and the flavor asymmetry in the sea quark distributions observed in Drell-Yan experiments. However, despite the various phenomenological successes of nucleon models which incorporate mesonic degrees of freedom, as yet there is scant experimental evidence unambiguously pointing to the existence of a mesonic cloud in high energy reactions. This experiment is designed to provide a clear signal of the presence of mesonic degrees of freedom in nucleon DIS, measuring where the pion contribution to the nucleon structure function should appear (i.e at relatively small Bjorken  $x \sim 0.1$ ), while simultaneously measuring the well-know DIS cross sections. Data from this experiment will, therefore, provide valuable input into high energy phenomenology and global fitting efforts for parton distribution functions by providing the size of the non-perturbative structure that needs to be addressed.

It is important to note also that this experiment may prove critical to a wide swath of the already-approved Jefferson Lab science program. There are multiple experiments planning to reach the factorization regime in semi-inclusive processes to access for instance transverse momentum dependent parton distribution functions as well as other semi-inclusive deep inelastic scattering physics such as flavor decomposition of the nucleon and single spin asymmetries. These experiments seek to measure at kinematics where the current fragmentation region may be cleanly separated from a target regime described as a nucleon via the well-known parton distribution functions. This latter aspect is not a valid approach if target fragmentation, as described by the fracture functions, is not also considered as a production mechanism as well that will impact the yield of measurable hadrons. Here, the mesonic component of the nucleon is likely for example to play an important role in final state interactions. Therefore, the proposed measurement may provide information valuable to precise interpretation of the underlying phenomena involved in a host of semi-inclusive scattering experiments in the Jefferson Lab 12 GeV era.

Moving into the future, the tagging approach pioneered here for probing the fracture

functions may pave the way for programs to map out the non-perturbative, mesonic, component of the nucleon both at Jefferson Lab in the 12 GeV era and at the proposed EIC, mEIC, and LHeC colliders. In the near term, this experimental approach could be leveraged further to tag semi-inclusive scattering such as  $ep \rightarrow ep\pi X$ , or to probe the strange quark content via  $ep \rightarrow e\Lambda X$ . At higher energies, the hard diffractive scattering measurements at HERA demonstrate the wealth of interesting physics specifically in the regime of these proposed new colliders. Because of the typically small cross sections, high luminosity as well as dedicated tagging detectors will be required; these are currently being included into electron-ion collider planning. Such measurements will complement as well new Drell-Yan data that will become available from experiments at COMPASS and Fermilab, and also possibly at the J-PARC facility. In all, this proposed Jefferson Lab experiment will provide a permanent, lower energy anchor for a wealth of future experiments.

## 1.5 Physics Motivation Summary

- A new and rigorous formalism of fracture functions, or conditional parton distributions, has been introduced to extend the usual QCD picture of semi-inclusive deep inelastic processes to the low momentum region of phase space where the target fragmentation contribution becomes important. This experiment will provide a first high precision measurement of the fracture functions.
- The measurement of the isospin dependence ( $p$ - $n$  difference) of the conditional PDFs would settle the question of the relative importance of singlet and non-singlet exchanges in target fragmentation, which cannot be answered from the high-energy data alone.
- A large component of the approved JLab 12 GeV physics program, in particular semi-inclusive measurements to access processes such as TMDs, flavor decomposition of the nucleon, single spin asymmetries, and the like could ultimately be rendered difficult to interpret cleanly due to effects coming from the target fragmentation region which are typically not considered. This experiment will measure such effects.
- Few experiments have been able to directly probe the partonic components of the meson cloud of the nucleon, basically only scant data from hard diffractive processes at HERA and Drell-Yan to date. A range of models and theoretical work that predict the size and components of this cloud are available, but little data exists to constrain them.
- Measuring the "recoil" proton at low momentum will facilitate extrapolation to the pion pole term, thereby facilitating a measurement of the pion structure function via the Sullivan process. The partonic structure of the pion, the lightest and simplest hadron, is not well measured over the entire Bjorken- $x$  range and the predictions of models describing pion structure differ significantly. There is a great need to measure the pion structure function with a new and independent technique.

- The well established quark flavor asymmetry in the nucleon sea can be explained in terms of the meson cloud model. The Sullivan process allows access to the meson cloud of the nucleon, and direct measurement of this component will facilitate checks on the validity of this interpretation.
- The measurements of the pion parton distribution in the Drell-Yan (Fermilab E615 and possibly at COMPASS in the future) is limited to charged pions. The proposed experiment will measure both the charged and neutral pion. This will facilitate a check of the validity of isospin symmetry. Generally, the complementarity of the  $p \rightarrow p$  and  $n \rightarrow p$  reactions will assist in the identification of pion exchange and other contributions.
- The nucleon structure function has been measured to multiple orders of magnitude precisely in  $x$  and  $Q^2$ . The standard description is given by valence quarks which radiate gluons, thereby generating sea quarks - all well described by DGLAP evolution. However, some part of the measured structure function data ( 20% in total) comes from scattering not from valence or sea quarks as described this way, but rather from bound mesonic or meson-like objects in the nucleon. This experiment will provide a direct measure of a part of this effect, tagging the latter while simultaneously measuring the former.
- The measurement of tagged DIS at HERA explored diffractive scattering and extracted the pion parton distribution at small  $x$  and rather large  $Q^2$  . At JLab, one can measure this at larger  $x$  and smaller  $Q^2$  – advantageous kinematics for evolution between the two experiments.
- This is a gateway experiment to a broad program, in the near term at Jefferson Lab and in the far term at an electron-ion collider, to map out the non-perturbative, mesonic content of the nucleon and study target fragmentation.

## 2 Experiment

### 2.1 Overview

We propose to measure the semi-inclusive reactions  $H(e, e'p)X$  and  $D(e, e'pp)X$  in the deep inelastic regime of  $8 < W^2 < 18 \text{ GeV}^2$ ,  $1 < Q^2 < 3 \text{ GeV}^2$ , and  $0.05 < x < 0.2$ , for very low proton momenta in the range 60 MeV/c up to 400 MeV/c. The key to this experimental technique is to measure the low-energy outgoing "recoil" proton (as well as a very low energy spectator proton in the D case) in coincidence with a deeply inelastically scattered electron, as shown for example in Fig. 20. The inclusive electron kinematics determine that a DIS event has occurred, i.e. that the reconstructed  $Q^2$  and missing mass,  $W^2$ , of the recoiling hadronic system are sufficiently large. However, unlike the standard inclusive case, the low momentum protons  $N'$  measured in time and vertex coincidence with the DIS event ensure that the deep inelastic scattering occurred from partons within the meson cloud (here depicted as a pion) surrounding the nucleon. This can be achieved by employing the Super Bigbite Spectrometer to detect the scattered electrons in time and vertex coincidence with low momentum proton(s) measured in a low mass radial time projection chamber (RTPC, a BONUS-like detector).

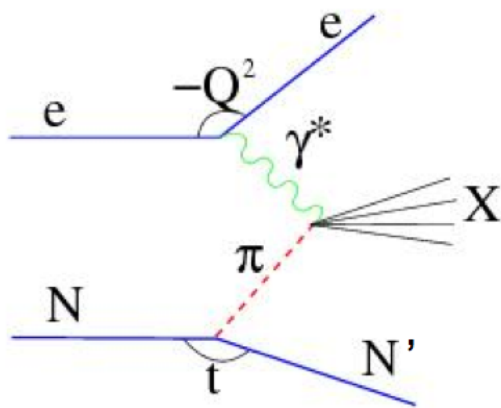


Figure 20: Feynman diagram for electron scattering from the pion cloud of the nucleon  $N$ , with the initial nucleon at rest.

### 2.2 Experiment Luminosity

The subject of the proposed experiment is an essential feature of the proton internal structure, specifically, a quark-quark correlation related to the meson cloud associated with a (fluctuating/recoiling) nucleon. In spite of enormous developments in the field of nucleon structure over the last 65 plus years since the original Fermi and Marshall 20% number was given for the pion-nucleon component of the nucleon wave function, this estimate endures without significant change. However, the experimental signature of the pion in the nucleon remains under debate.

A fixed-target experiment at kinematics with modest momentum transfers and higher  $x$  will compliment the already performed HERA experiments which investigated diffractive



## Electron arm – SuperBigbite

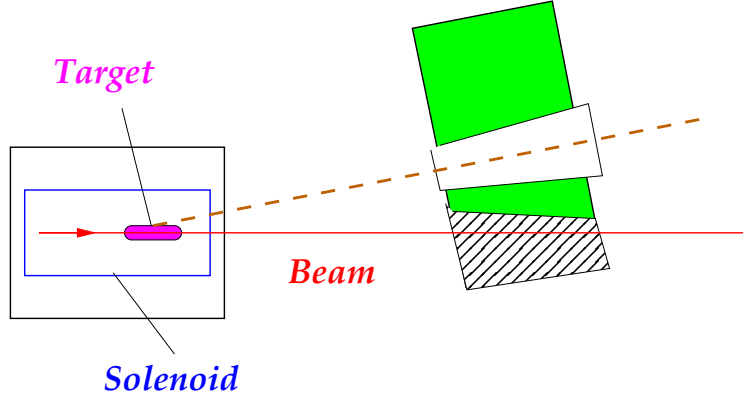


Figure 21: Schematic layout of the proposed experiment.

DIS in a collider regime with an 800 GeV proton beam on a 30 GeV positron beam. The proposed study of TDIS through detection of a very low energy proton "tag" in coincidence with a scattered electron DIS event will measure a very different part of the reaction space, one that may be rigorously evolved to the HERA kinematics, as well as related to the long-searched-for Sullivan process for accessing the pion structure function.

In this section we present a set of considerations concerning the Figure-of-Merit (FOM) for this experiment, a product of electron-nucleon luminosity ( $\mathcal{L}$ ), electron detector acceptance ( $\Omega_e$ ), and recoil proton detection efficiency ( $\eta_p$ ), required for TDIS investigation. The level of luminosity which may be used in the proposed experimental setup is constrained by the signal size and, critically, the experimental background rates.

The cross section of the inclusive DIS process for an 11 GeV electron beam scattered from a proton target is very well known, see e.g. the PDG report [88]. A traditional measurement of the DIS cross section with 1% precision and minimal DIS requirements on  $Q^2$  and  $W^2$  does not require much time with any electron spectrometer at Jefferson Lab, and experiments have been approved that will extend the existing body of such data in this kinematic regime from SLAC and other laboratories. The (unmeasured) percentage in total of such events coming from the meson cloud of the proton target should be approximately 20%. However, the fraction of DIS events in coincidence with a **low energy** proton is much smaller than the total meson-nucleon part of the wave function. According to recent calculations, as above, the fraction of DIS events with proton momenta below 400 MeV/c and at an angle within the detector acceptance (above  $30^\circ$ ),  $F_{\pi p}(x_{Bj}, \Delta k, \Delta\theta)$ , is about 0.1% [89] (see Fig. 22).

Such a small fraction leads to a low rate of true coincidence events between the DIS-scattered electron and the recoiling, target proton. Therefore, the proposed experiment requires a large FOM and good control of accidental coincidences. The high rate of accidental coincidence events is the main problem for measurement of the TDIS cross section. These events are mainly due to a large rate of low energy protons produced in low momentum transfer reactions, such as small angle electron elastic scattering and meson photoproduction. In the deuterium target, one needs to also consider deuteron

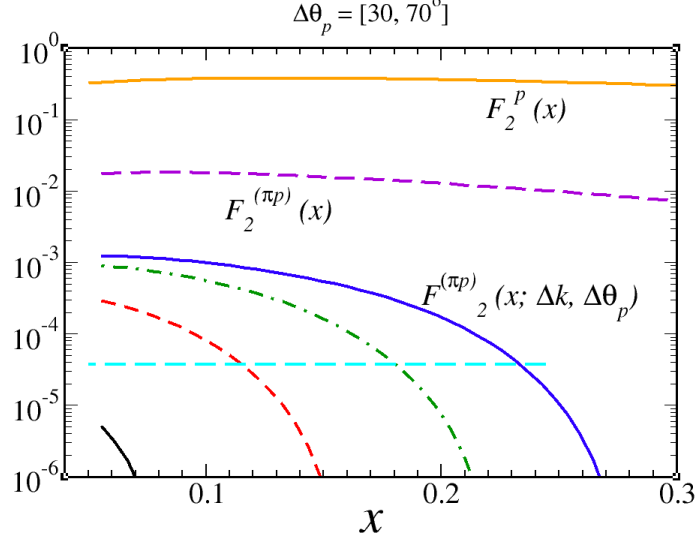


Figure 22: The proton SF  $F_2^p$ , the pion related part  $F_2^{(\pi p)}$ , and the fraction  $F_2^{(\pi p)}(\Delta k, \Delta \theta_h)$  vs  $x$  for the proton momentum intervals,  $\Delta k$ : in MeV/c - black (60-100), red (100-200), green (200-300), blue (300-400) and the cut on the angle between the proton and the virtual photon momentum directions,  $\Theta_p$ , between  $30^\circ$  and  $70^\circ$ . The dash cyan line shows the level of fracture functions which could be measured with 5% or better statistical accuracy in a ten-day run at an electron-nucleon luminosity  $3 \times 10^{36} \text{ cm}^{-2}/\text{s}$ .

photodisintegration into low momentum proton-neutron pairs and the wider angular distribution of the protons involved in quasi-elastic electron scattering. There are four parameters which allow rejection of the accidental protons:

- The polar angle between the proton track and the beam direction.
- The correlation in time between an electron hit in the SBS and a proton hit in the RTPC.
- The correlation between the vertices of the electron and proton tracks.
- The correlation between the vertex of the spectator proton (tagging the neutron as a target, as in BONUS) and the recoil proton for the deuterium target.

**Accidental Rates (Hydrogen Case)** There is a very high total rate of low momentum protons from low energy elastic electron-proton scattering. In the momentum range  $k > 70 \text{ MeV}/c$  and luminosity  $3 \times 10^{36} \text{ cm}^{-2}/\text{s}$ , the rate is about 170 MHz. However, these protons scatter predominantly in the angular range  $78 - 88^\circ$ . In comparison, the proton data of interest will be in a range only up to  $65^\circ$  maximum. The projected polar angle resolution of the RTPC of  $1^\circ$  will allow rejection of the range of angles where most elastically scattered protons are located. The background rate in the angular range  $\theta_p < 70^\circ$  is relatively small (200 kHz), and we will place a cut at this angle value.

The photoproduction mechanism leads to a higher rate, which was found to be 3 MHz from the hydrogen target at the proposed luminosity of  $3 \times 10^{36} \text{ cm}^{-2}/\text{s}$  in the momentum

and angular range of interest. For additional information about this background, see the discussion of background simulations, below, in this proposal. The projected time resolution of the RTPC of 10 ns allows for a narrow 20 ns timing cut in offline data analysis. A significant length of the RTPC target cell (40 cm), combined with the good vertex resolution of the SBS spectrometer, will provide additional suppression of accidental events by a factor of 10. The resulting total accidental probability is expected, then, to be **0.003** for  $H(e, e'p)X$  events.

**Accidental Rates (Deuterium Case)** For the deuterium target at the same electron-nucleon luminosity of  $3 \times 10^{36} \text{ cm}^{-2}/\text{s}$ , there will be a large additional background rate coming from photo-disintegration protons,  $\sim 40 \text{ MHz}$  in the momentum range below 250 MeV/c. Moreover, there will be an even larger rate of the quasi-elastically produced protons,  $\sim 85 \text{ MHz}$ . This combined rate of 125 MHz complicates investigation of TDIS from the neutron at low proton momenta. After cutting on the angular range of interest the rate is expected to be  $\sim 45 \text{ MHz}$ , which leads to an accidental event probability of **0.02** per DIS electron. However, in the proton momentum range above 250 MeV/c the rate of protons drops dramatically. The combined rate of protons in the angular range of interest is about 10 MHz. The resulting accidental probability is expected, then, to be **0.005** in  $D(e, e'pp)X$  events.

The projected level of the signal to accidental rate varies with  $x$ . For illustration purposes, we show in Fig. 23 the event distribution over  $\delta z = z_p - z_e$  after other cuts are applied for a level of signal to background ratio of 1/10. The  $\delta z$  range represents the 40 cm target length, and it is important to note that the background events will be produced evenly along the target. In contrast, the data will be produced at a single vertex that we propose to measure with an accuracy of 8 mm.

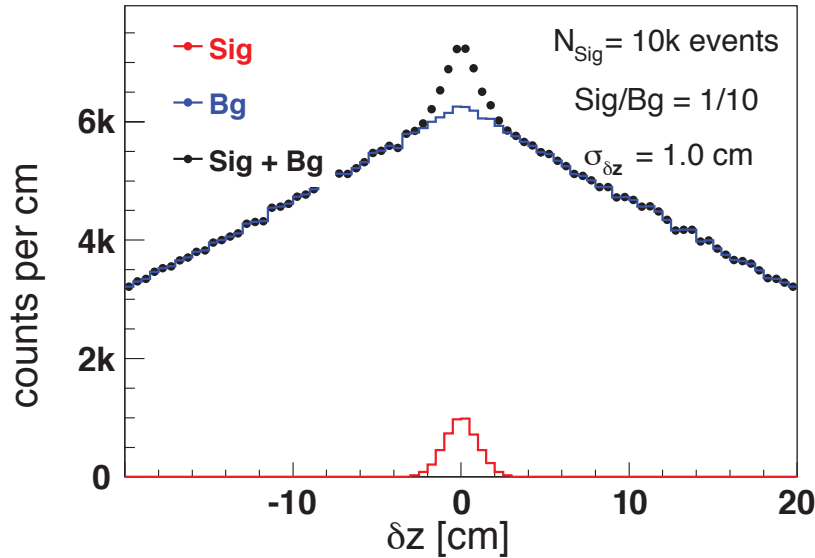


Figure 23: The projected event distribution over  $\delta z = z_p - z_e$  for a ratio of signal to background of 1/10 (in the "2- $\sigma$ " area).

For verification of the analysis procedure and measurement at higher  $x$  up to 0.16 where the expected rate of e-p events is smaller (see Fig. 14), we plan to reduce the luminosity to  $\lesssim 1 \times 10^{36} \text{ cm}^{-2}/\text{s}$  and collect data for an additional period of 5 days. It is at these kinematics that the projected drop in the meson cloud distribution, and consequently in the fracture function, should be most apparent.

## 2.3 Recoil Detector

Detection of a soft nucleon is complicated by a large intensity of the secondary electrons, photons, and soft nucleons produced in the interaction of the high energy electron beam with the target. A proton detection option has several essential advantages over neutron detection, as were leveraged by the BONUS and CLAS eg6 experiments:

- The ionization density in the soft proton track for the momentum range 60-400 MeV/c is very high, which allows effective suppression of the secondary electron and soft photon induced signals.
- The protons of interest (2.0 - over 30 MeV kinetic energy) have a momentum component perpendicular to the beam direction much larger than the typical perpendicular momentum of the secondary electrons, which allows use of magnetic separation of the proton and electron background using a solenoidal magnet.
- The proton track allows for reconstruction of the event vertex and direction, which are powerful means for rejection of accidental events.
- The proton detector readout segmentation could be on the level of  $10^5$  or above, which is at least a factor of 100 times higher than practical for a neutron detector.

The recoil detector will be fundamentally the same as the cylindrical RTPC being developed for the experiment to measure the structure function of the free neutron (E12-06-103, or BONUS-12), the latter being based on the very successful cylindrical RTPCs that were employed for the BONUS and CLAS eg6 experiments as pictured in Fig. 24. The proposed RTPC will, however, utilize a different solenoid. This is an existing solenoid, shown in Fig. 25, with a 400-mm warm bore, a total length of 152.7 cm, and a superconducting coil that operates with a 47 kG magnetic field in the center of the magnet. This solenoid belongs to the UVa collaborators on this proposal, and is currently being used for tests of LHC detector electronics. Simulation studies have shown that increasing the radial drift region by a factor of 2 compared to the BONUS and eg6 RTPC detectors can provide at least a 50% relative improvement in the momentum resolution, as well as extend the momentum range of the detector. The larger bore of this magnet will facilitate the RTPC having a larger radial drift distance than that proposed for BONUS-12. The enhanced drift region will facilitate measurements of proton momenta up to 400 MeV/c with a resolution of 3%. The length of this magnet is also a help, allowing us to use a longer (40 cm) target for improved background rejection and luminosity.

The proposed TDIS RTPC will be 40 cm long and consist of an annulus with inner radius of 5 cm and an outer radius of 15 cm. The amplification of the drifting electrons will be achieved by three layers of cylindrical Gas Electron Multiplier (GEM, see Ref. [90])

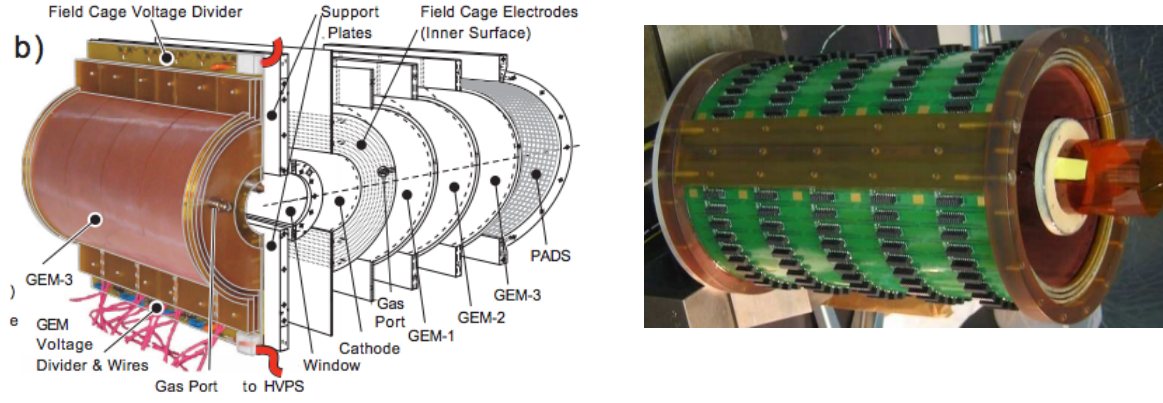


Figure 24: (left) Photograph of the BoNuS RTPC, showing the left module with the readout padboard removed and a complementary exploded view exposing the components of the right module. (right) Photograph of the eg6 RTPC during assembly.

foils at radii of 15 cm. This will be surrounded by a cylindrical readout surface featuring elongated pads. GEMs are  $50\text{ }\mu\text{m}$  thick polyamide foils coated on both sides with a  $5\text{ }\mu\text{m}$  copper layer and punctured with  $70\text{ }\mu\text{m}$  holes. The distance between these holes is about  $140\text{ }\mu\text{m}$ . By applying a voltage in the range of 200 V to 300 V across the two copper layers a very high electric yield is formed inside the holes. Ionized electrons from the maximally ionizing low momentum protons drifting towards the GEM foil produce an avalanche of secondary electrons when captured and accelerated through the holes. The total gain in GEM will be of the order of  $10^3$ , which is far below the limit of gain achievable with GEM-based detectors. The electrons are transferred to the next GEM foil and, after passing three GEM foils, the resulting electron pulse will be detected on the readout plane. The full length of the RTPC could be closer to 60 cm to accommodate protons emitted at angle as small as  $30^\circ$  relative to the beam direction.

As with BONUS and CLAS eg6, materials between the target and the sensitive detector volume have to be minimized to prevent energy loss of the protons and to minimize the interaction of background particles which reduce efficiency of magnetic confinement of the low energy background. The tracking region will be formed by a set of light weight straws, a set of wires, and the GEM. The straws will hold a  $2\text{ }\mu\text{m}$  gold plated kapton film cylinder. The wires will be used to increase the electrical field at a larger radius. To further minimize background events, a thin wall Be tube will be used for the first 50 cm of the beam line downstream from the target. After that a larger, standard Al pipe will provide connection to the exit beam line through the SBS magnet to the beam dump. The window between the low pressure, cold RTPC and atmosphere will be made from a pre-deformed 0.5 mm aluminum plate with a supporting grid of steel bars. The recent design of a cylindrical GEM chamber at INFN Frascati for the KLOE experiment [91] will be explored for potential improvements.

The RTPC will be filled with a He based mixture which allows reduction of the secondary background in the chamber due to low energy photon induced signals. A study of GEM operation with low pressure He-based mixture has been demonstrated in the reference [92].



The SRS system consists of the following components:

- APV-25 hybrid cards mounted on the detector. These cards contain the 128 channel APV-25 chip which reads data from the detector, multiplexes the data, and transmits analog to the ADC card.
- SRS ADC unit that houses the ADC chips that de-multiplex data and convert into digital format.
- SRS FEC card which handles the clock and trigger synchronization. A single FEC and ADC card combination has the capability to read data from up to 16 APV hybrid cards.
- Scalable Readout Unit (SRU), an optional component not shown in the figure, which distributes the clock and trigger synchronization to the FEC cards. One SRU handles communication between multiple (up to 40) FEC cards and the data acquisition computer.
- The data acquisition computer, which could be part of a larger DAQ system as one of the readout controllers.

Work is currently underway to incorporate the SRS system into the CODA data acquisition framework at JLab. Our plan is to be as compatible to the existing SBS GEM tracker module readout as possible.

### 2.3.1 Target cell

The proposed TDIS target inside the RTPC is significantly different from those previously utilized. The target vessel is here a cylinder with an inner radius of 5 mm and 40 cm long. The target will be gaseous Hydrogen or Deuterium at 77 °K and 1 atm. In order to minimize the energy loss of the protons of interest, we have reduced the material of the target wall as much as possible, down to 10 micrometers of aluminum. The larger diameter of the cell and the aluminum walls are necessary given the high luminosity of the proposed experiment. The lower temperature of the target (liquid nitrogen) and increased length of the cell allow reduction of the gas pressure in the target (from 7 atm used in BONUS) to 1 atm.

The resulting threshold and energy loss for low energy protons are presented in Tab. 1, as calculated by our Geant4 Monte Carlo model of the RTPC. This is a modification of the Monte Carlo successfully utilized to analyze the BONUS experiment. Fig. 26 shows the RTPC in this Monte Carlo, which includes also the proposed solenoidal magnetic field as can be seen by the track curvature.

The actual energy loss through the target gas and walls, as well as through the various materials in Tab. 1, depends on the proton track angle when encountering the material. Fig. 27 depicts Monte Carlo results for protons escaping the target, demonstrating this angular dependence for initial proton angles as well as the minimum momentum threshold ( $\gtrsim 56$  MeV/c) for the experiment. These threshold particles just barely penetrate the cathode.

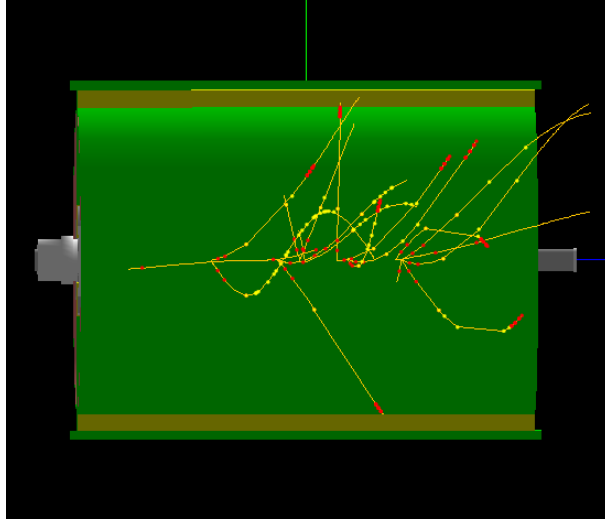


Figure 26: Side view of the RTPC as simulated by the Geant4 model of the proposed experiment.

### 2.3.2 RTPC Calibration

The proposed measurement of the tagged DIS cross section will require good knowledge of the various detector acceptances and efficiencies. The fully inclusive electron-proton and electron-deuteron cross sections are well known from experiments in this kinematic regime at Jefferson Lab and SLAC [93]. Comparing our untagged DIS measurements with these data will allow for precision checks of the acceptance, efficiency, and other corrections used for the SBS electron spectrometer analysis.

The RTPC will also require study and calibration. The BONUS experiment was not able to make precise acceptance and efficiency corrections to the RTPC data to measure the neutron cross section directly using the tagging technique, but rather had to simulate as well as normalize to a model  $F_2^n/F_2^d$  ratio for an assumed-known kinematics within the data set. This contributed significantly to the uncertainty of the measurement [94]. We could perhaps employ a similar approach, but suggest also that different quantities may be used as well to extract the RTPC acceptance and efficiency.

Some initial calibration can be done by using the copious proton tracks from elastic electron-proton scattering. At production luminosity there will be several accidental elastic proton tracks distributed evenly along the target for in every  $e - p$  DIS event. These protons are well separated from the protons of interest because, to be at the same momentum but generated by elastic events, they are necessarily kinematically directed almost perpendicular to the beam.

It will be particularly productive to use quasi-elastic electron scattering from the deuteron for the RTPC calibration. The energy and direction of the spectator proton may be determined in a quasi-elastic reaction using a scattered electron in the SBS in combination with a neutron measured with the (relocated) SBS Hadron Calorimeter (HCAL). The moveable HCAL detector would not be a part of the SBS for this experiment, and could be placed beam right at optimum kinematics to record neutrons for this calibration



p(MeV/c)	50	75	100	150	225	325
$E_{kin}$ (MeV)	1.33	3.00	5.31	11.9	26.6	54.7
90 deg						
at TargetWall	1.24	2.95	5.28	11.9	26.6	54.7
after TargetWall	0.75	2.71	5.13	11.8	26.6	54.7
after Cathode		2.43	4.97	11.7	26.5	54.6
at 1st GEM			4.47	11.6	26.4	54.6
45 deg						
at TargetWall	1.21	2.93	5.27	11.9	26.6	54.7
after TargetWall	0.45	2.59	5.06	11.8	26.5	54.6
after Cathode		2.11	4.82	11.7	26.5	54.6
at 1st GEM				11.4	26.4	54.6

Table 1: Monte Carlo results for kinetic energy loss of protons starting at the indicated momenta on top line, presented for various positions as the protons encounter structures while radially traversing the RTPC.

measurement. In such a way we can predict the distribution of protons of energy, for instance 5-27 MeV (100-225 MeV/c), in the directions required for the RTPC calibration. A comparison between the measured proton spectra and the proton distributions expected in the RTPC from quasi-elastic neutrons in HCAL will provide a check on the RTPC proton acceptance and efficiency corrections. If the suggested quasi-elastic HCAL neutron measurement is for some reason not available to the proposed measurement, it will be possible though not optimal to work through simulation and geometry as was done for the CLAS6 experiments.

The proposed calibration will be performed at an electron-nucleon luminosity of  $0.3 \times 10^{36}$  Hz/cm<sup>2</sup> with an electron beam energy 4.4 GeV and SBS angle at the same angle of 12 degrees as during the production TDIS run. Projected rate of electron-neutron quasi-elastic events in SBS is of 1000 Hz. The average neutron momentum will be 970 MeV/c. Using HCAL located at a distance of 15 meters (60 degrees relative to the beam direction) we estimated that the coincidence  $e - n$  rate will be approximately 70-80 Hz. Neutron momentum will be within a cone with an average angle relatively the beam of 60° and the opening of  $\pm 4^\circ$ . At such a low luminosity the spectator protons will be easy to identify and use for RTPC calibration. One day of such a measurement provides more than 6 million events of tagged protons which allow detailed study of RTPC.

## 2.4 The Super Bigbite Spectrometer

The Super Bigbite Spectrometer (SBS), currently under construction and fully funded by DOE NP, consists of a dipole and a modular detector package. An important feature of the SBS is a beam path through the opening in the right side yoke of the magnet, which allows it to be placed at forward angles as small as 3.5°. For the proposed experiment the SBS magnet (front face of the yoke) will be placed 2.0 m from the target allowing

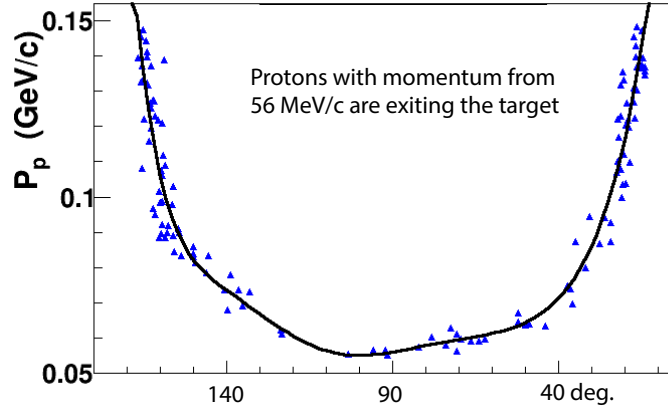


Figure 27: Minimum proton momentum as a function of angle for protons exiting the RTPC target.

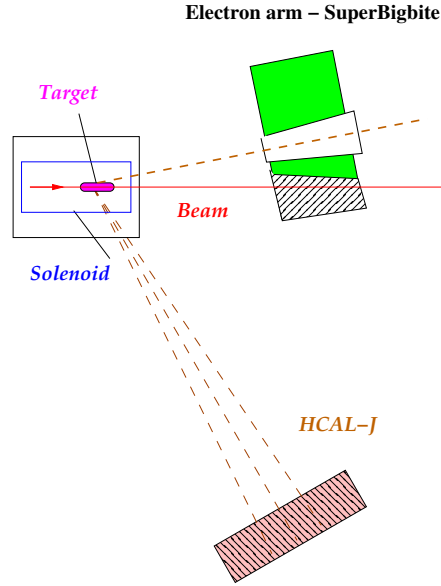


Figure 28: Setup for RTDC calibration

for a 50 msr solid angle around a  $12^\circ$  central angle. The large out-of-plane angle of SBS provides significant coverage in azimuthal angle (about 20% of  $2\pi$ ). Figure 30 shows the spectrometer solid angle vs. scattering angle for such a setting. In the proposed experiment we plan to use the large GEM-based chambers currently under construction for the SBS  $G_E^p$  experiment polarimeter as the main tracking planes. We plan to use five out of ten constructed planes and concentrate the readout electronics of all ten planes in those five. These chambers will each cover a 60 cm x 200 cm area, and the concentrated electronics will then allow reading of every readout strip. These chambers were tested in such a configuration and a spatial resolution of 60-70  $\mu\text{m}$  was obtained.

The combination of an electromagnetic calorimeter (the CLAS-6 Large Angle Calorime-

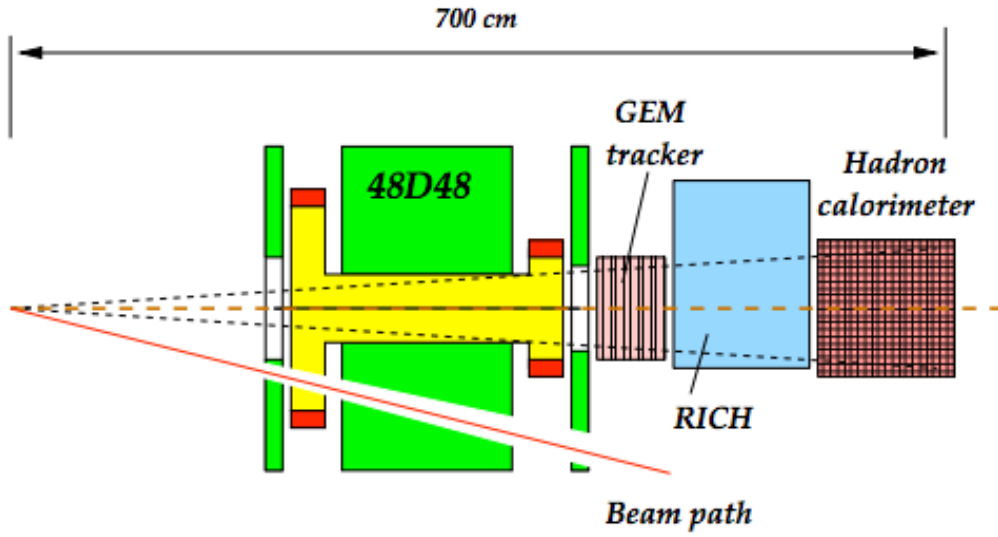


Figure 29: Schematic of the Super Bigbite Spectrometer

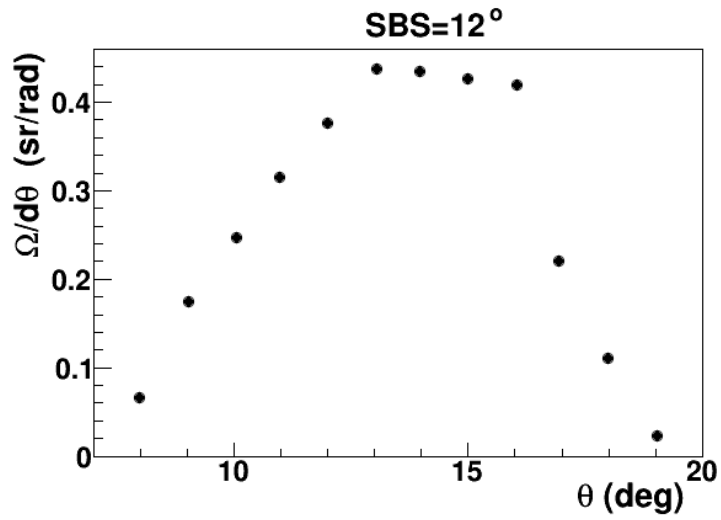


Figure 30: Solid angle vs. polar angle at the 12° SBS position.

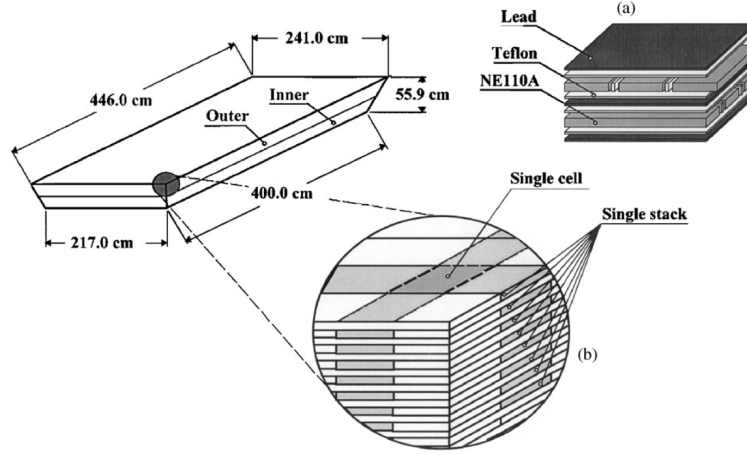


Figure 31: The conceptual drawing of the internal structure of the LAC module.

ter or LAC) and threshold gas Cherenkov counter (the HERMES RICH or GC-SBS) will be used for trigger and particle identification purposes. The LAC is discussed in some detail below. The Gas Cherenkov will be a straightforward modification of the existing ring imaging Cherenkov (RICH) detector planned to be utilized in the approved SBS experiment E12-09-018 - basically filling the tank with  $\text{CO}_2$ . The combination of these two detectors will be sufficient for the electron particle identification purposes of this experiment.

#### 2.4.1 CLAS6 Large Acceptance Calorimeter

The SBS was originally designed to be a hadron spectrometer. In order to use SBS as an electron spectrometer with good pion rejection capability we will replace the hadron calorimeter with the safely salvaged Large Acceptance Calorimeter (LAC) from the CLAS6 detector.

The conceptual drawing of the internal structure of the LAC is shown in Fig. 31. The LAC module has a rectangular shape with a sensitive area of  $217 \times 400 \text{ cm}^2$  and consists 33 layers, each composed of a 0.20 cm thick lead foil and 1.5 cm thick NE110A plastic scintillator bars. The total thickness is about 12.9 radiation lengths or 1 hadronic absorption length. Each scintillator layer is protected from contact with the lead by 0.02 cm thick Teflon foils. The width of the scintillators is roughly 10 cm and is slightly increasing from the inner layers toward the outer layers to provide a focusing geometry. Scintillators in consecutive layers are rotated by 90 degrees to form a  $40 \times 24$  matrix of cells with area approximately  $10 \times 10 \text{ cm}^2$ . The module is vertically divided into two groups: an inner (first 17 layers) and an outer (16 layers) groups. Each group has its own light readouts. Scintillators lying one on top of the other with the same orientation form a stack. For each stack the light is collected at both ends separately using light guides coupled to EMI 9954A photomultiplier tubes. For each module there are 128 stacks and 256 photomultipliers [96].

The LAC energy resolution for electromagnetic showers is  $7.5 \pm 0.2 \%$  [96]. Combined with CLAS, the pion contamination is less than 1% for cuts that give a detection efficiency

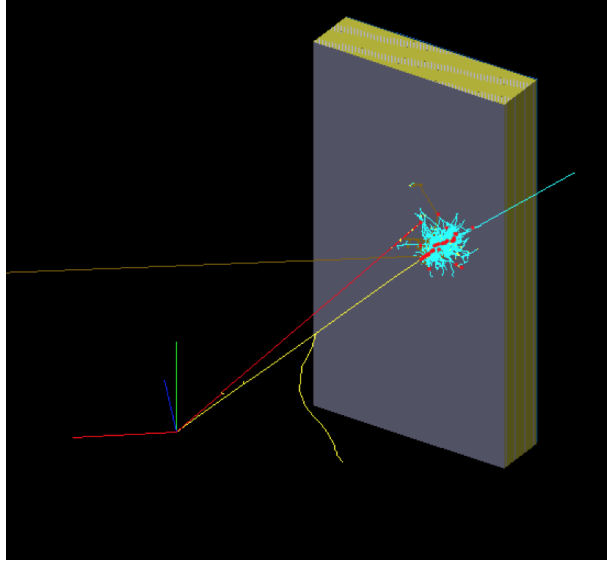


Figure 32: The LAC in the Geant4 Simulation. The red trajectory is a pion and the yellow is an electron.

of 95% for 2 GeV electrons.

A Geant4 simulation has been performed to study the LAC for this proposal. Fig. [32] shows the LAC in this Geant4 program. Our results indicate that grouping the first 17 layers into the inner part should provide a good choice and that the particle identification cut should include two parts:  $E_{tot}/P > 0.33$  and  $E_{in}$  cuts. Here,  $E_{tot}/P$  is the fraction of energy deposited in the LAC compared to the total momentum of the particle, and  $E_{in}$  is the energy deposited in the inner layers only. The optimum cut value for  $E_{in}$  is momentum dependent. The results indicate that the pion rejection fractions will be 89%, 92%, 95% and 96.5% for particles with momenta 1.0, 2.0, 5.0 and 8.0 GeV/c, respectively.

#### 2.4.2 Super Bigbite Trigger and DAQ

It is proposed that the Level-1 trigger will be formed using the total energy deposition in the LAC and the Level-2 trigger will use correlation between the coordinates of the signals in the LAC and GC-SBS and energy deposition information in two layers of LAC. The RTPC will be readout for any kind of trigger.

**Pipeline Electronics** For the SBS experiment GEP the proton trigger is achieved digitally using the Jefferson Lab Lab pipeline electronics. All of the 288 channels of the hadron calorimeter (HCAL) are continuously sampled at 250 MHz. The data of each block is sent to a crate trigger processor where the clustering algorithm computes the sums of 16 adjacent blocks and produces a trigger if one cluster is above threshold. This process takes about 700 ns. Once the trigger is generated, the data from the FADC is looked back up in the pipeline memory to be read out. Since the LAC has only 216 channels we propose to reuse the ECAL trigger electronics and readout to generate the single shower trigger. The singles shower trigger will also be prescaled in order to study the Cherenkov counter efficiency.

**Large Angle Calorimeter** The Large Angle Calorimeter is constituted of layers of scintillator and lead. For this experiment the sensitive area will be limited to 1.8m x 3.6m to match the SBS acceptance. The detector is arranged in two parts, the front part containing 16 layers and the back part containing 17 layers. This corresponds to a total number of 256 PMTs. For the LAC PMTs summing we plan to reuse electronics of the ECAL calorimeter (an electron arm of the GEP experiment). The energy deposited in two layers of the calorimeter will be estimated by summed signals of adjacent paddles. First, we produce the overlapping sums in the both layers. It would be 58 signals for the layer-1 and 58 for the layer-2. Then the signals of two layers will be combined. Resulting  $19(X) + 39(Y)$  analog signals will be discriminated and form (via logical OR) a Level-1 trigger. These 58 logical signals will be used in the FPGA scheme for geometrical match of the pulses in GC-SBS and LAC as a part-1 of the Level-2 trigger. The 19 analog signals from each layer will be analyzed by using the three FADC modules for suppression of the charge pion events as a part-2 of the Level-2 trigger.

**SBS Cherenkov Detector** In order to suppress the trigger rate originated by pions and photons, we are planning to modify the RICH counter under commissioning for the SBS transversity experiment. It will require removal the aerogel (or blocking light from it) with  $\text{CO}_2$  and using it as a threshold Cherenkov detector. The RICH counter has an array of 2000 PMTs as it will be used in the approved SBS transversity experiment. A 8(x2) channel amplifier discriminator board was developed by Glasgow University based on the NINO chip. Using discriminated signals provided by this board, with the amplitude over threshold of the signal integrated in the width of the logic signal, we would need 125 boards. Resulting 250 logical pulses will be used in the FPGA scheme for summed areas of geometrical match.

**GEM Tracker Electronics** The GEM signals for the multiple SBS tracking planes will be read using the APV25 readout and the SRS system as described above. This will be used for the RTPC in the same way that it is currently planned for the GEM trackers of Super Bigbite.

## 2.5 Simulations of the Radial Time Project Chamber

Two MC Geant models were used. The first was developed for the Bonus experiment and adjusted in our case for acceptance investigation and some material studies to ensure low proton momenta. The second was developed specifically in this proposal for complete investigation of the background issues.

The impact of beam-related background processes on the RTPC has been assessed using a simulation based on the latest version of Geant-4 (4.10.0.p01). The simulation considers (Fig.33) a “straw” target of radius 5 mm and length 400 mm, held in a 10  $\mu\text{m}$  thick Al cylinder, with 20  $\mu\text{m}$  Be end windows, and filled with 2 atm of  $\text{H}_2$  or  $\text{D}_2$  gas. This is surrounded by the He gas of the RTPC, at a pressure of 0.05 atm (0.15 atm @ 77°K), contained within a volume of 150 mm radius. Both the straw target and the He volume are maintained at a temperature of 25°K or 77°K. A ring of 12.7  $\mu\text{m}$  radius W field wires divides the He volume into an insensitive region (He-inner) at radii  $r < 50$  mm and a sensitive region (He-outer) at radii  $50 < r < 150$  mm. Ionization produced in He-outer is swept by the radial electric field to an outer ( $r > 150$  mm) triple GEM detector with

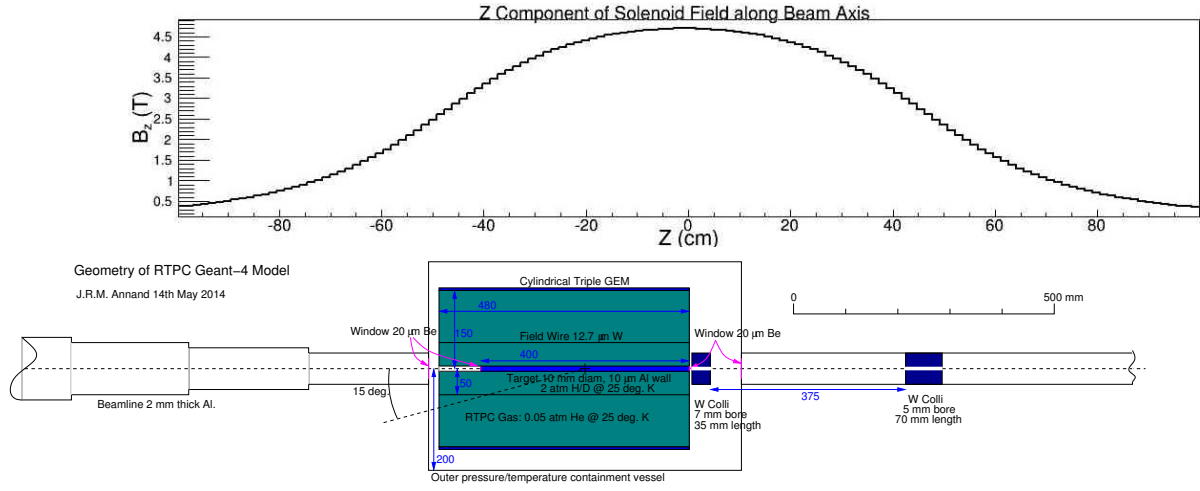


Figure 33: Side view of the simulation geometry, which includes the magnetic field map of the S3 (UVa) solenoid.

pixel readout.

Operating with the target at 25°K and 2 atm, an electron beam current of  $\sim 50 \mu\text{A}$  will produce a luminosity of  $10^{37} \text{ cm}^{-2}\text{s}^{-1}$ , reducing to  $3.2 \times 10^{36} \text{ cm}^{-2}\text{s}^{-1}$  if the target is operated at 77°K. At these luminosities a large background will be generated in the vicinity of the target. This comes mainly from Moeller scattering of the incident electrons, with smaller contributions from bremsstrahlung and pair production. Most of the background electrons have low energy and are confined inside the sensitive region of the RTPC by the solenoid magnetic field.

Fig. 34(A) shows the radial distribution of energy deposited in the target and RTPC for different magnetic field strengths. The calculation has been made with  $5 \times 10^7$  incident 11 GeV electrons, for uniform fields of 1.0, 2.0, and 4.0 T, as well as the “S3” solenoid field map (Fig. 33) calculated in TOSCA. In the region of the target the maximum S3 longitudinal field is in excess of 4 T. As the field strength is increased the rate of decent of energy loss, with respect to radius, becomes steeper in He-inner. However there remains a background in He-outer which is not suppressed by increasing the field strength. A small fraction,  $\sim 5 \%$ , of this can be attributed to intermediate bremsstrahlung in the target region, followed by pair production. However most originates from interactions of the beam downstream from the target (Fig.33). It is thus important that the magnetic field extends well beyond the target and that the beam line has sufficiently large diameter to accommodate the increasing lateral spread in the exit beam. The present calculation has the exit beam line as stepped periodically to larger radii as one travels downstream from the target. Increasing the expansion of the exit beam line beyond that depicted in Fig. 33 has an insignificant effect on the He-outer background if an electron beam radius of 0.5 mm is used. The integrated energy loss in He-outer has some dependence on the beam-line material, but 2-4 mm thickness Al gives reasonable results. Upstream from the target a dual W collimator is installed to suppress increased background produced by an off-axis beam. Fig. 34(B) shows the radial energy distribution, with the S3 field map and different 2 atm gas targets. The mean energy losses per incident 11 GeV electron

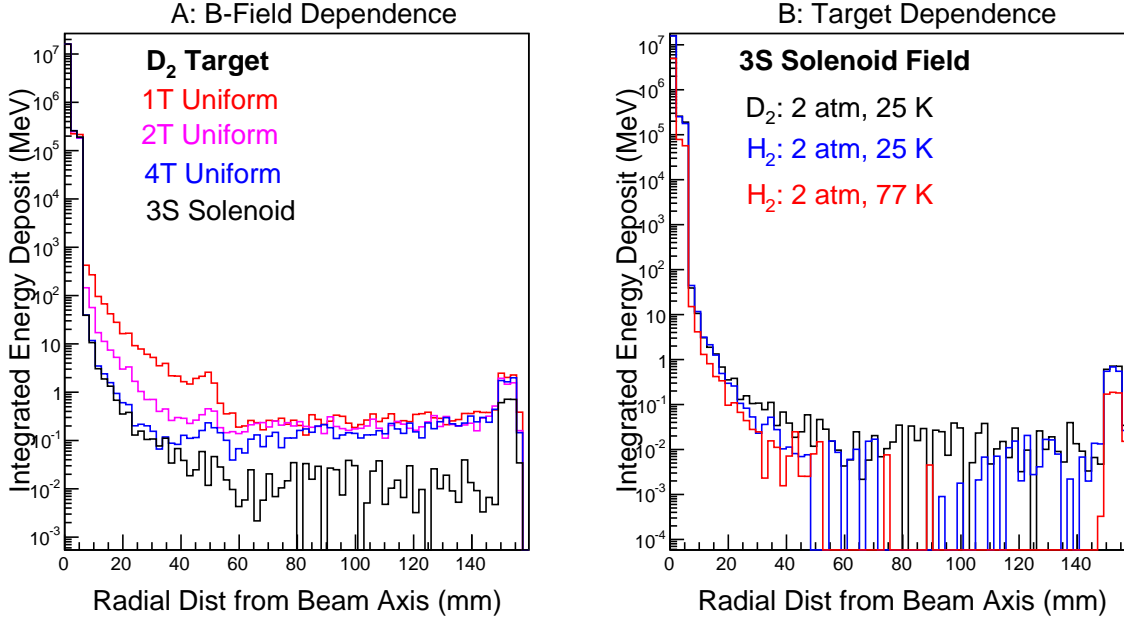


Figure 34: A: confinement of Moeller energy deposit for a 2 atm, 25°K target and various magnetic field configurations. B: S3 solenoid field map and different targets. Simulations have  $5 \times 10^7$  incident electrons of 11 GeV energy.

Target	Mean $E_{dep}$ (MeV) $r \leq 5$ mm	Mean $E_{dep}$ (MeV) $5 < r \leq 15$ mm	Probability
$D_2$ , 25°K	0.33	$0.41 \times 10^{-7}$	$5 \times 10^{-7}$
$H_2$ , 25°K	0.32	$0.36 \times 10^{-7}$	$3 \times 10^{-7}$
$H_2$ , 77°K	0.10	$0.11 \times 10^{-7}$	$1 \times 10^{-7}$

Table 2: Electromagnetic background calculations for  $H_2$  and  $D_2$  targets operated at 2 atm pressure. The magnetic field is S3 solenoid.

are given in Table 2. Column “ $r \leq 5$  mm” gives the mean energy loss in the target and He-inner and column “ $5 < r \leq 15$  mm” the mean energy loss in He-outer.

The MC generated data have also been analyzed on an event-by-event basis and column “Probability” of Table 2 gives the probability of an electron event in the sensitive region where the mean  $dE/dx$  along the electron track exceeds 0.2 keV/mm. Protons of interest would be expected to produce a larger  $dE/dx$ . Taking for example the case of  $H_2$  at 25°K, a 50  $\mu$ A incident beam would produce a detectable rate of  $9 \times 10^7$  Hz in the sensitive area. This would contribute to the occupancy of the readout pads in the GEM detector, but the electron track loci are quite different from those produced by protons.

Fig. 35 compares the transverse distribution of energy deposited for electrons (A) and protons (B). In A outside of the central region, there are  $\sim 5$  tracks (equivalent to  $10^{-7}$  probability per incident beam electron) which would reconstruct as originating from the target, with a radius of curvature consistent with  $p \sim 250$  MeV/c and -ve charge. The outer ring of energy deposit is from photon conversion in the GEM detector. In B the



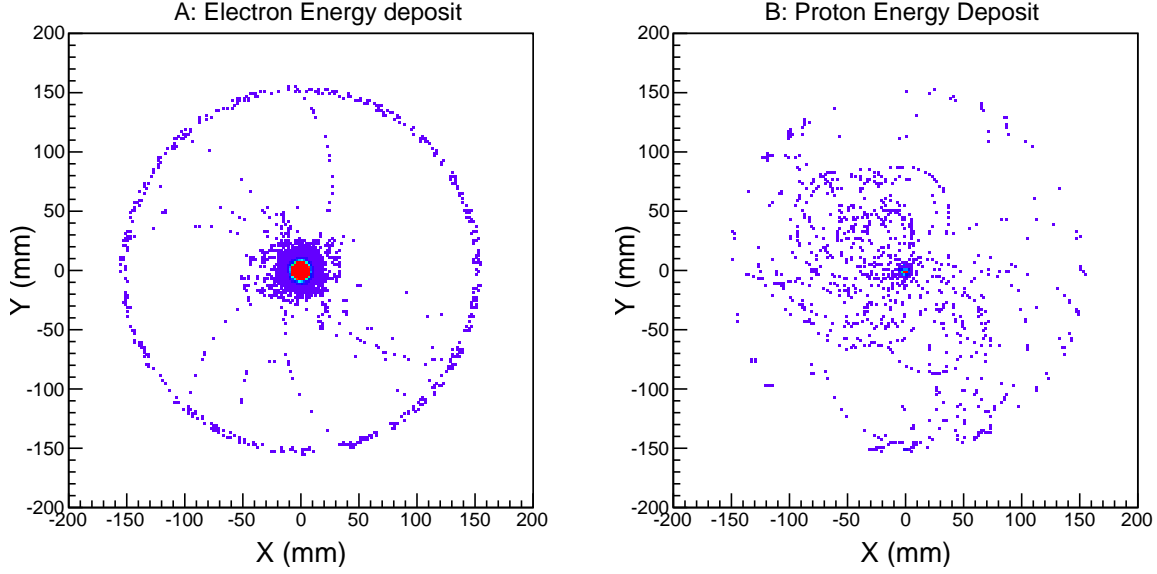


Figure 35: A: radial dependence of integrated energy loss for electrons, B: for photo protons.

photo proton tracks originate from the target region. For the deuterium target relatively large numbers of low momentum protons are produced as shown by the tightly curved tracks of radius a few cm.

Although electromagnetic processes are the dominant source of background, electrons impinging on the He-outer sensitive region generally have a relatively low energy loss, compared to the low-momentum protons of interest to recoil tagging. Photo nuclear processes, on the other hand, have much lower cross sections, but will produce significant numbers of highly-ionizing protons in a similar momentum range to those of interest. These protons will not be suppressed by the solenoidal field. Calculations have been made with the present simulation using the “extended electromagnetic” physics list of Geant-4 which includes photo- and electro-nuclear processes. Hadronic processes of produced nucleons and mesons are also included.

Fig. 36 compares the energy distributions of photo protons produced in the  $H_2$  and  $D_2$  targets. The number of generated photo protons and their distribution in energy is consistent with a calculation made by the “DINREG” code, which is based on Geant-3 and has been used previously to estimate the intensity of background processes in Hall A. Integrated over  $4\pi$ , each incident 11 GeV electron has a probability of producing a photo proton of  $\sim 10^{-6}$ . The deuterium distribution has a much larger peak at low energy ( $T_p < 20$  MeV) in the region of interest for tagged structure functions. This, and the different proton angular distributions from  $H_2$  and  $D_2$  has a major effect on the background which impinges on recoil-tagging kinematics.

Fig. 37 compares the angle and momentum of photo protons produced in  $H_2$  and  $D_2$  targets. The  $H_2$  distribution is skewed to higher momenta (as in Fig. 36) and also to more forward angles. Thus cuts to select the recoil-tagging region of interest ( $p_p < 250$  MeV/c,  $30 < \theta_p < 70^\circ$ ) have a much larger effect on the  $H_2$  photo proton background rate. Table

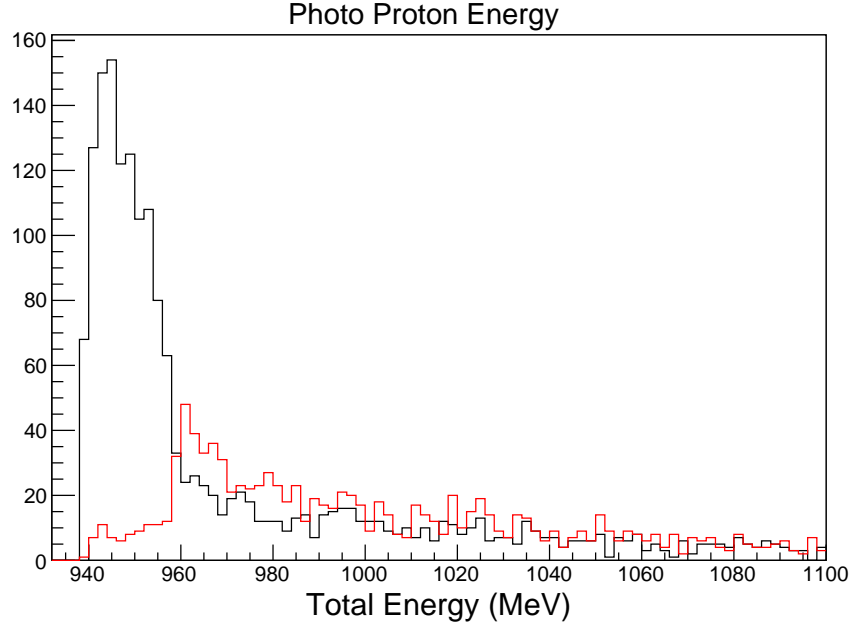


Figure 36: Energy dependence of protons produced in the target by background photo nuclear processes.

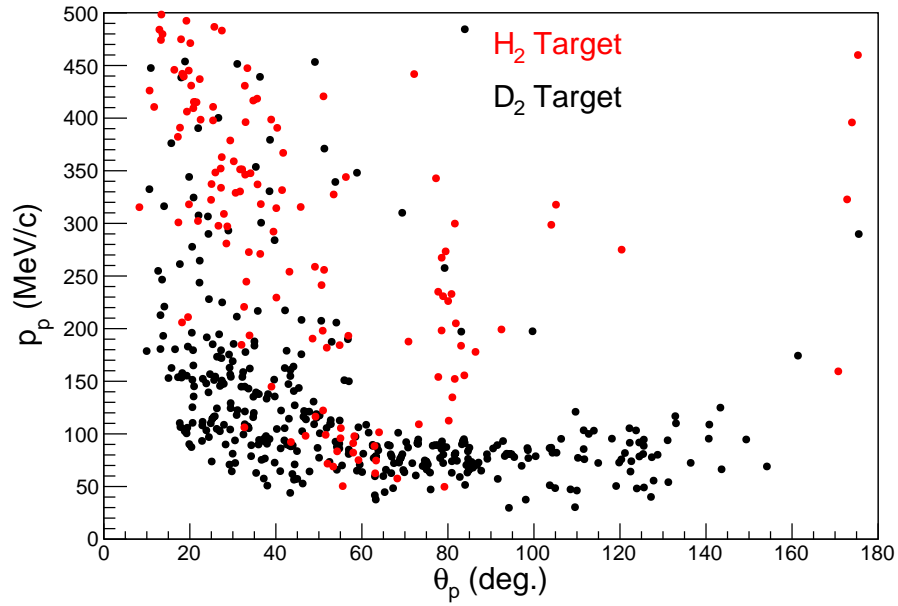


Figure 37: Comparison of momentum and angle dependence of photo protons produced in  $H_2$  and  $D_2$  targets and detected in He-outer (the RTPC tracking volume).

40 cm, 77°K 1 atm pressure	All protons	All protons $p_p < 250 \text{ MeV/c}$	He-outer no cuts	He-outer $p_p < 250 \text{ MeV/c}$	$p_p < 250 \text{ MeV/c}$ $30 < \theta_p < 70^\circ$
Hydrogen	$2.8 \times 10^{-7}$	$5.4 \times 10^{-8}$	$3.0 \times 10^{-8}$	$1.0 \times 10^{-8}$	$0.57 \times 10^{-8}$
Deuterium	$3.6 \times 10^{-7}$	$2.2 \times 10^{-7}$	$6.6 \times 10^{-8}$	$5.8 \times 10^{-8}$	$2.4 \times 10^{-8}$

Table 3: Photo proton production/detection probabilities per incident 11 GeV electron. The target thicknesses are for operation with 60  $\mu\text{A}$  beam at electron-nuclei luminosity of  $3 \times 10^{36} \text{ cm}^{-2}/\text{s}$ . Production run on the deuterium target will use 30  $\mu\text{A}$  beam intensity.

3 shows the effect of applying such cuts, in terms of the probability of detecting a proton per incident 11 GeV electron.

### 2.5.1 Kinematics

For the purpose of understanding the kinematics of the experiment, we also generated electron scattering events using a simpler, basic Monte Carlo with a flat distribution in  $Q^2$  from  $1.0 - 10.0 \text{ GeV}^2$ , and a flat distribution in  $x_B j$  from 0.001 to 0.5. The electron energy and angle are calculated and events are kept for electron angles between 5 and 45 degrees, and electron energies above 0.25 GeV.

The recoil proton was generated with a flat momentum distribution from 10 MeV to 400 MeV, a flat distribution in  $\cos(\theta)$  from 5 to 165 degrees, and a flat  $\phi$  distribution across  $2\pi$ . There is no explicit cut on transverse momentum  $p_T$  with respect to the photon direction.  $z$  is calculated as the ratio of the 4-momentum product of the recoil proton and photon to that of the initial proton and photon, so  $z$  is the 4-momentum fraction of the fluctuated proton longitudinal with the photon.  $z$  is required be between 0.8 and 0.98, so the accepted  $y_\pi$  values are from 0.02 to 0.2.

The splitting function is calculated as a function of  $y_\pi$  and  $p_T$ , and is required to be greater than zero. The  $t_\pi$  is required to be above -0.2 and below the proton  $t_{min}$  limit as defined above.  $x_\pi$  is defined as  $x/(1 - z)$ , and is required to be between 0.0 and 0.99. Finally, the pion DIS cross section is calculated as a function of  $x_\pi$  and  $Q^2$ , neglecting off-shell effects, and using pion parton distributions in CERNLIB.

Fig. 38 depicts the electron scattering angle and energy  $E'$  range remaining after the cuts. The smaller the  $z$  range, the smaller the maximum  $E'$  for a given angle.

Fig. 39 depicts the recoil (target) proton momentum and angle range remaining after the cuts. It is important to note from the latter that the protons of interest to detect are in a range substantially less than 90 degrees. This is important, as the large background from elastic e-p scattering produces protons around a small cone 90 degrees from the scattering vertex. It will be possible to use reconstructed angle to separate the events of interest from those of the background. This will be more difficult for the deuterium measurement due to Fermi smearing.

A particularly nice result comes from looking at the projected data in  $t$  versus the pion momentum fraction  $y$ . In Fig. 40, the upper and lower red lines are the  $t_{min}$  for the Delta resonance according to Eq. 13, shifting the Delta mass by half the width. Here, a resonance width of 118 MeV was used, and so the upper and lower lines correspond to  $\pm 59 \text{ MeV}$ . The central line represents the Delta mass, with the black data, then, below and the blue above the Delta. Plotting the data this way should allow for a kinematic cut to cleanly isolate events which could not have come from an intermediate Delta state in the low proton momentum range of interest for extrapolation to the pion pole.

Fig. 41 shows the projected kinematics for the proposed experiment determined by the inclusive electron events. As noted earlier, the  $x$  range is determined by the low  $t$  range of interest, through the variables  $z$  and the low spectator momentum. This  $x$  range is, moreover, optimized for observation of pions events in the meson cloud. Once the  $x$  range is fixed, the  $Q^2$  range obtainable with the 11 GeV beam is also determined. While the latter is not very high, the kinematics are nonetheless clearly in the deep inelastic scattering regime – with  $W^2$  values typically between 10 and  $15 \text{ GeV}^2$ .

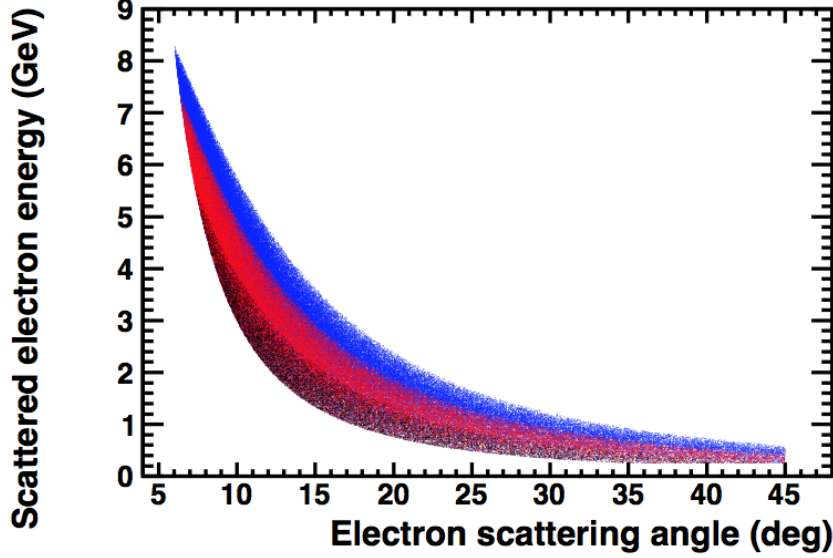


Figure 38: Scattered electron energy and angle dependence from the simple Monte Carlo. The blue points have  $z$  in the range 0.15-0.2, the red points have  $z$  in the range 0.10-0.15, and the black points have  $z$  in the range 0.05-0.10.

### 3 Projected Results

Fig. 42 is similar to Fig. 14 above for the hydrogen target, but with example projected data from this proposal added for the central momentum bin. The statistical uncertainty on the projected data is between 12% and less than 0.5% with the larger error being at the smallest cross section values where  $F_2^{(\pi p)}(x, \Delta|\mathbf{k}|, \Delta\theta_{p'})$  dramatically turns down in  $x$ . The data will be binned in both  $x$  and proton momentum bins such that *every* range in momentum shown will have the same full range of precision data as shown in the example. Fig. 42 depicts the pion, but it is important to note that the ratio of the measured tagged to untagged ratio **is** the fracture function. It is critical to point out that, regardless of isolation of the pion content, this experiment will provide a direct measurement of the fracture functions over a broad range of kinematics.

Using the momentum bins of Fig. 42, Fig. 43 depicts the potential reach for the  $t$  extrapolation of  $F_2^{(\pi p)}(t, \Delta x)$  towards the pion pole for one bin in  $0.09 < x < 0.11$ . The data will facilitate a similar extraction for *every*  $x$  bin proposed. Here, the low momentum reach of the RTPC detector is critical to define the downward-turning shape of the curve for extrapolation.

Fig. 44 is similar to Fig. 15, presenting the same structure function quantities for the neutron as were just shown for the proton, but with a comparison instead to the strength of other physics channels, the tagged structure functions for  $(\pi^- p)$ ,  $(\rho^- p)$ , and  $(\pi^0 \Delta^0 + \pi^- \Delta^+)$ , rather than to the measured momentum range components. The statistical uncertainty on the projected data is included, and ranges between 0.4 and 1.3%, with

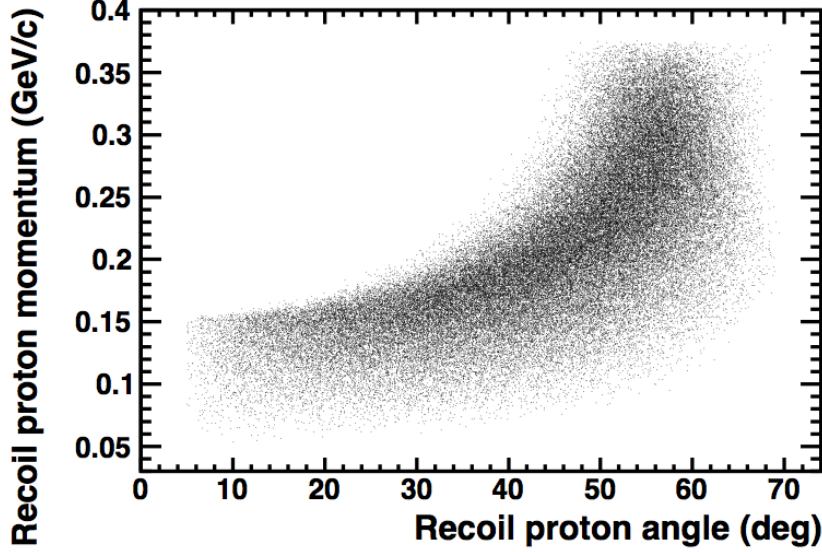


Figure 39: Recoil proton momentum and angle dependence from the simple Monte Carlo.

the larger error being at the smaller cross section, larger  $x$  values. Here, a momentum range from 250 – 400 MeV only is shown rather than the full requested range down to 150 MeV/c. It is not anticipated that we will measure below 150 MeV/c, due to the increased background constraints. The expected statistical uncertainty for the deuterium measurement in the momentum bin  $150 < k < 200$  MeV/c is 15%, moving to nearly  $\sim 1\%$  in the highest momentum bin. As with the hydrogen data, multiple bins in both momentum and  $x$  will be obtained.

The proposed experiment should as well provide access to the pion structure function via the Sullivan process, where the coincidence of the DIS-scattered electron and the low momentum recoil proton will tag a pion target event. Experimental knowledge of the partonic structure of the pion is currently very limited due to the lack of a pion target, and most of the current knowledge of the pion structure function in the valence region is obtained primarily from pionic Drell-Yan scattering [46]-[48].

Fig 45 shows the projected pion structure function that can be extracted from this experiment. A 24% systematic uncertainty in the pion flux is assumed. The projected results are shown along with the existing pionic Drell-Yan data from E615 and the GRV-p parametrization of the pion structure function, and a calculation based on the Dyson-Schwinger equation [53]. There are several theoretical calculations of the pion structure in the valence region, however they tend to disagree with each other – underscoring that it is essential to measure the pion structure function over a wide range of  $x$ .

As can be seen in Fig. 45, the proposed data nicely complement the Drell-Yan data and will fill in the heretofore unprobed moderate  $x$  range. Moreover and importantly, measurements of pion parton distributions using the Drell-Yan process are limited to charged pions, while the proposed experiment will also include the neutral pion and provide a check of the validity of isospin symmetry.

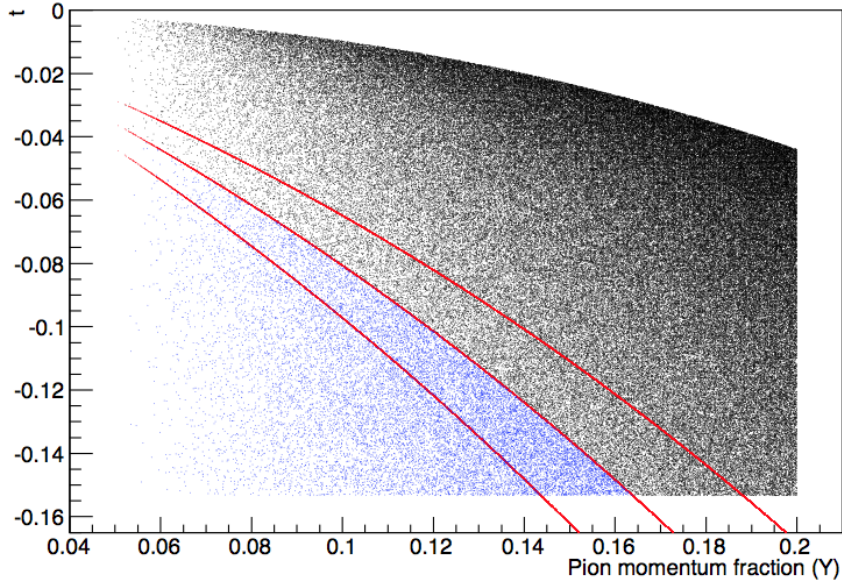


Figure 40: Accepted counts in  $t$  versus the pion momentum fraction  $y$ . The black data are below the minimum  $t$  for the Delta resonance, and the blue are above. The red lines are the central value for the Delta, as well as the Delta mass shifted up and down by half the width.

### 3.1 Beam Time Request

We propose to measure the semi-inclusive reactions  $p(e, e'p)X$  and  $D(e, e'pp)X$  using a  $50\mu\text{A}$  beam on a 1 atm, cooled straw, gaseous hydrogen target with radius of 5 mm and length of 40 cm, for a total luminosity of  $3 \times 10^{36} \text{ cm}^{-2}\text{s}^{-1}$ . The well-known DIS cross section was used as the initial basis for calculation [93], in conjunction with the rate due to the pionic contribution given by  $\text{Rate}(\text{DIS}_{\pi N}) = \text{Rate}(\text{DIS}) \times (F2_{\pi N}/F2_n)$  from the calculations presented in the Motivation section of this proposal [89]. The Tagged-DIS rate on hydrogen is given by  $\text{Rate}(\text{TDIS}_{\pi N}) = \text{Rate}(\text{DIS}) \times \text{eff}_{\text{RTPC}} \times \text{eff}_{\text{SBS}}$ , using a conservative combined RTPC efficiency and acceptance of 40% and SBS efficiency of 90%. The  $x$  range  $0.06 < x < 0.2$  will be divided into 5 bins and, for *each* bin in  $x$ , the recoil proton momentum  $k$  will be divided into at least another 6 bins. The requested beam time is estimated with the goal of better than 1% statistical uncertainty on average for the recoil momentum  $k$  bins within each  $x$  bin. The worst case scenario is the lowest rate, highest  $x$  bin, where we estimate that 10 days of beam time is needed to obtain adequate statistical precision. Due to the large acceptance of the SBS and RTPC, all of the other remaining data displayed and projected will be obtained *simultaneously* with this bin and so require no additional beam time request.

Table 4 shows the estimated electron cross section within the SBS acceptance, the  $F2_{\pi N}/F2_n$ , the projected TDIS rate, and the yield in each  $x$  bin for 10 days of beam on a hydrogen target. Table 4 also shows the yield in each  $x$  bin for 5 days of beam on a deuterium target. The requested time is smaller here because it is not anticipated that we will measure the lowest momentum proton bin, below 150 MeV/c, due to the

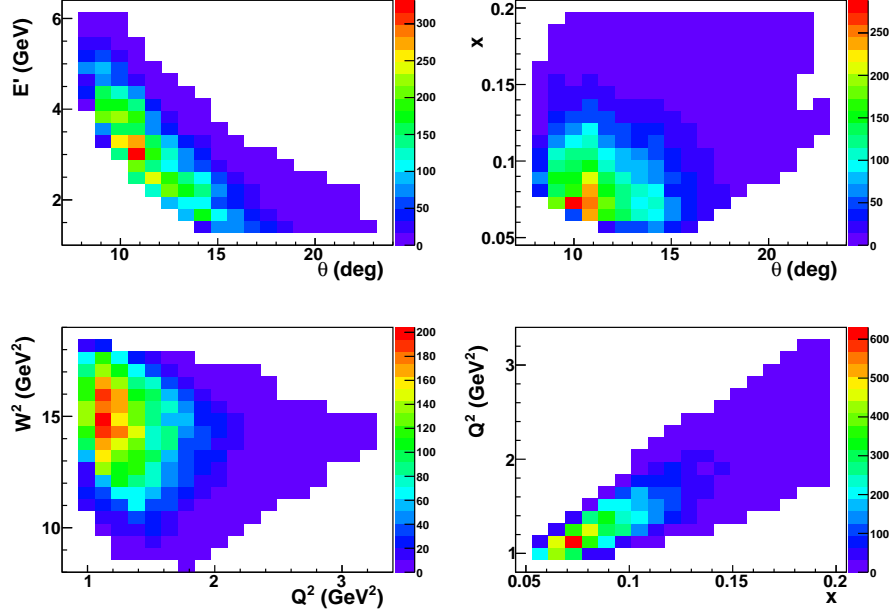


Figure 41: Kinematics for the proposed experiment, as indicated, determined by the inclusive electron events.

increased background constraints. The expected statistical uncertainty for the deuterium measurement in the momentum bin  $150 < k < 200$  MeV/c is 15%, moving to nearly  $\sim 1\%$  in the highest momentum bin. The requirement of two low momentum protons detected in vertex and time coincidence (one backward and one more forward) requires double-accounting for the RTPC efficiency when using the deuterium target – which is very conservatively estimated here. Each kinematic  $E', \theta, \phi$  bin must pass cuts on the SBS acceptance, and an electron trigger energy  $< 6$  GeV, and threshold  $> 1$  GeV are required. There are also kinematic cuts employed to ensure  $W > 2$  and  $Q^2 > 1$  GeV<sup>2</sup>.

Table 5 shows the estimated statistical uncertainty,  $\delta\sigma/\sigma$  in percent, for the proton momentum bins ( $\Delta k$ , top) to be measured *within an  $x$  bin* around  $0.1 \pm 0.01$  for the hydrogen target, as an example for the momentum range and breadth of data expected within *each* of the  $x$  bins in Table 4. The range of momentum bins will directly provide a corresponding range of  $t$  bins for each  $x$ . Here, the electron and proton yields,  $N_{e,e'}$  and  $N_{e,e'p}^{good}$ , are subject to the same cuts and efficiency assumptions as in Table 4, above. The accidental rates  $N_{e,e'p}^{acc}$  are calculated as discussed in the Background section of this proposal, above, and the projected signal to noise ratio (S/N) is taken into account in calculating the expected statistical accuracy.

In addition to 10 days of 11 GeV beam on hydrogen and 5 days on deuterium, we request also 5 days on a hydrogen target at a reduced luminosity in order to validate the background subtraction procedure. It will be necessary to commission the RTPC, the new SBS electron detection system, as well as to verify the vertex and reconstruction optics. We request 2 beam days (mixed evenly between the the hydrogen and deuterium targets), also at 11 GeV, for these requisite preparations. We note that the collaboration anticipates some advance detector pre-commissioning of the RTPC and SBS detectors



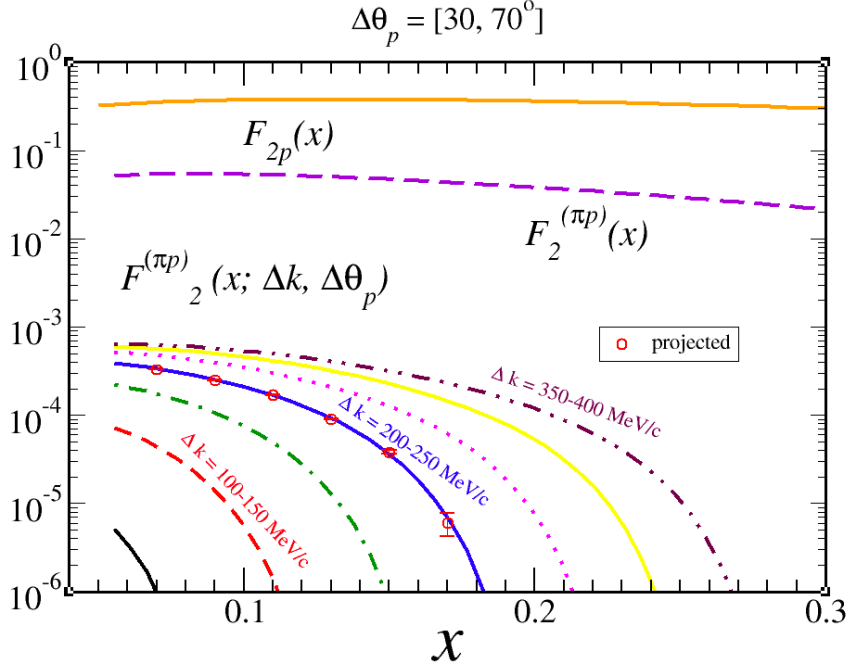


Figure 42:  $x$  dependence of the semi-inclusive structure function  $F_2^{(\pi p)}(x, \Delta|\mathbf{k}|, \Delta\theta_p)$ . The lower bands follow from varying the integration range  $\Delta|\mathbf{k}|$ ; they correspond to  $\Delta|\mathbf{k}| = [60, 100]$  MeV (black, solid),  $\Delta|\mathbf{k}| = [100, 150]$  MeV (red, dashed),  $\Delta|\mathbf{k}| = [150, 200]$  MeV (green, dot-dashed),  $\Delta|\mathbf{k}| = [200, 250]$  MeV (blue, solid),  $\Delta|\mathbf{k}| = [250, 300]$  MeV (pink, dotted),  $\Delta|\mathbf{k}| = [300, 350]$  MeV (yellow, solid), and  $\Delta|\mathbf{k}| = [350, 400]$  MeV (purple, dot-dashed). For comparison, the total integrated  $\pi p$  contribution  $F_2^{(\pi p)}$  to the inclusive proton structure function is shown (violed dashed), as is the total inclusive  $F_{2p}$  structure function (orange solid). The data are example projections for this experiment for the central bin. Similar data will be obtained for *every* momentum bin shown.

using radioactive sources, cosmic rays, and possibly the low energy proton beam at TUNL as was done in advance for BONUS. Lastly, two shifts of beam time at 4.4 GeV will be required for measuring the RTPC acceptance and efficiency using elastic neutrons measured in HCAL, as described above. The two shifts are planned to take place one at the start of the deuterium running and one at the end to track any time-dependent systematic effects. This will require two half-shift beam energy changes, where target gas changes will take place concurrently. The total beam time request of 23 days is summarized in Table 6.

### 3.2 Expected Experimental Accuracy

An overall systematic uncertainty of 5% in the cross section measurements is assumed for this experiment, building on the CLAS-6 BONUS and eg6 experience utilizing the RTPC [94]. We believe this to be highly reasonable for the following reasons. First, CLAS-6 had a large ( $> 5\%$ ) uncertainty associated with the  $E, \theta$  dependent CLAS trigger

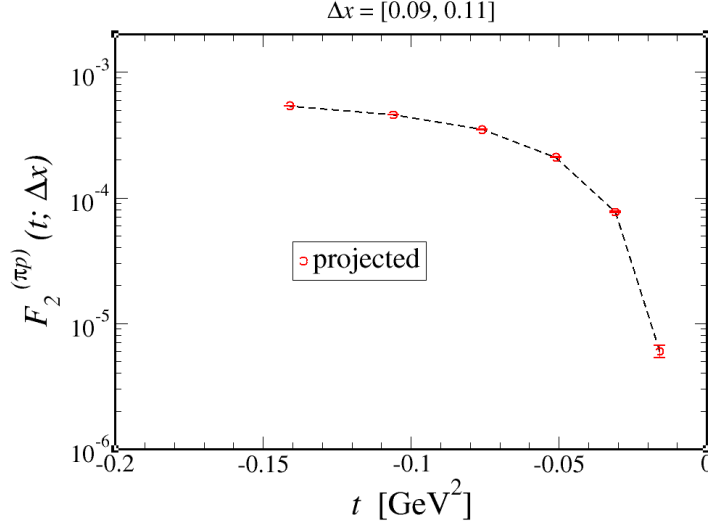


Figure 43:  $t$  dependence of  $F_2^{(\pi p)}(t, \Delta x)$  for momentum bins between 100 and 400 MeV/c, in steps of 50 MeV/c, in one projected  $x$  bin of  $0.09 < x < 0.11$ . Statistical error bars are included, but difficult to see on the log scale.

efficiency. The SBS is a far simpler device, and is expected to have a very small trigger efficiency uncertainty and only a 3% overall systematic uncertainty. In BONUS, moreover, 4.2% of the 8.7% overall systematic uncertainty came from the inclusive  $F_2^d/F_2^p$  model dependence in the ratio measurement performed – largely in the resonance region. We are here proposing a cross section measurement, with no ratio normalization technique to be employed. SBS inclusive results can be verified against the well-known proton DIS cross section. Moreover, the better spatial resolution of the proposed GEM readout, combined with the increased drift distance, will improve tracking and vertex resolution in the RTPC as compared to BONUS. We also propose not only to use a Monte Carlo for the RTPC acceptance and efficiency, but to carefully measure it using the HCAL elastic neutron technique described above.

## 4 Summary

We propose a pioneering measurement technique for probing the elusive mesonic content of the nucleon structure function. The technique involves detecting a low-momentum recoil proton (pair of protons) in coincidence with a deeply inelastically scattered electron from a hydrogen (deuterium) target. By tagging events from bound objects in the target, this technique provides a probe of the meson cloud component in the nucleon, and thereby access to the meson structure function. Additionally, this experiment will measure for the first time the conditional structure function, or fracture function, for proton and neutron targets in the target fragmentation region. The measurement will be performed in the  $Q^2$  range of 0.5 to 6 (GeV/c)<sup>2</sup> at very low proton momenta in the range of (60 – 400) MeV/c. The experiment will use the Super Bigbite Spectrometer to detect the scattered electrons

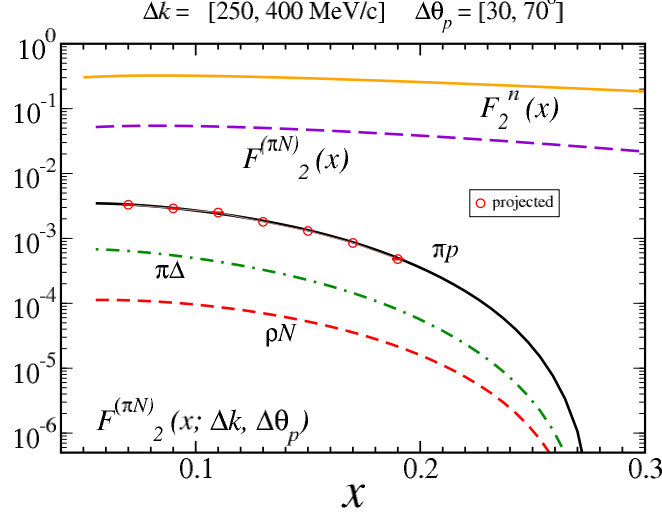


Figure 44: Structure functions as in Fig. 15 for the neutron-tagged target, with the  $x$  dependence of  $F_2^{(\pi p)}(x, \Delta|\mathbf{k}|, \Delta\theta_p)$  for charge-exchange in, e.g., the  $n \rightarrow \pi^- p$  process. The tagged semi-inclusive structure function for  $(\pi^- p)$  (black, solid),  $(\rho^- p)$  (red, dashed), and  $(\pi^0 \Delta^0 + \pi^- \Delta^+)$  (green, dot-dashed) are compared with the inclusive structure function of the neutron  $F_{2n}(x)$  (orange), and the fully-integrated  $(\pi^- p)$  contribution  $F_2^{\pi N}(x)$  (violet, dashed). Projected data are shown, with statistical error bars included.

and a low mass radial time projection chamber (RTPC, a BONUS-like detector) to detect the low momentum proton(s) in time and vertex coincidence with a DIS electron. In this experiment a  $50\mu$  A, 11 GeV beam will be incident on a 5 mm radius, 40 mm long straw tube target with 1 atm cool hydrogen (deuterium) gas. We request a total of 22 days of beam time, with 10 days of production  $50\mu$ A beam on the hydrogen target, 5 days production on the deuterium target, 2 days for optics and detector commissioning, and an additional 5 days of  $5\mu$  A beam on the hydrogen target for background checks.

x range	$\sigma_e$ in SBS (nb)	$F_2^{\pi N}/F_2$ ( $\times 10^{-5}$ )	TDIS $\pi N$ Rate (Hz)	Yield H <sub>2</sub> 10 days (k)	Yield D <sub>2</sub> 5 days (k)
0.06 - 0.2	1.84	116	2.31	1993	399
0.06 - 0.08	0.22	336	0.80	688	138
0.08 - 0.10	0.29	230	0.71	614	123
0.10 - 0.12	0.30	137	0.45	390	78
0.12 - 0.14	0.29	69	0.21	184	37
0.14 - 0.19	0.67	13	0.10	83	17

Table 4: Rates and expected yields for this experiment in the proposed  $x$  bins. All of the data will be obtained simultaneously for each target within the acceptance(s) of the SBS and RTPC without changing settings. Multiple proton momentum bins will be obtained within each  $x$  bin, as shown in the example below.

$\Delta k$ (MeV/c)	100-150	150-200	200-250	250-300	300-350	350-400
$\Delta T$ (MeV)	7	9	12	15	17	20
$N_{e,e'} (\times 10^6)$	710	710	710	710	710	710
$N_{e,e'p}^{good} (\times 10^3)$	4.6	59	159	267	354	413
$N_{e,e'p}^{acc} (\times 10^3)$	300	380	510	640	724	852
S/B	1/65	1/6.4	1/3.2	1/2.4	1/2	1/2
$\delta\sigma/\sigma$ (%)	12	1.1	0.5	0.4	0.3	0.3

Table 5: Statistical uncertainty for this experiment in an example  $x$  bin around  $0.1 \pm 0.01$  for the hydrogen target. It is planned that each proposed  $x$  bin will be broken down into such  $k$  bins, and that all of the data will be obtained simultaneously for each target within the acceptance(s) of the SBS and RTPC.

Target	Current ( $\mu A$ )	Beam Energy (GeV)	Beam Time (hrs)	Notes
Hydrogen	50	11	264	includes 1 day for commissioning
Deuterium	25	11	144	includes 1 day for commissioning
Hydrogen	5	11	120	RTPC calibration with HCAL Beam Energy Changes
Deuterium	5	4.4	16	
			8	
Total			552	23 days

Table 6: Summary beam time request, as described.

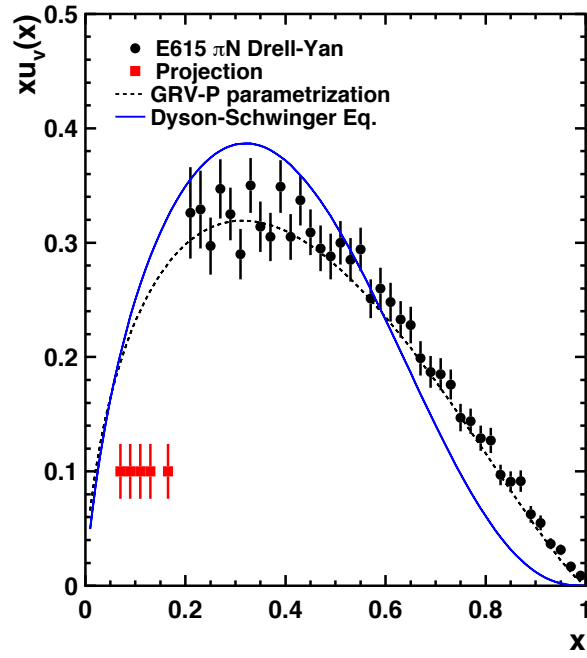


Figure 45: Projected pion structure function results. Also shown are the results from the pionic Drell-Yan experiment E615, the GRV-P parametrization and a Dyson-Schwinger equation based calculation from Ref. [53]

# References

- [1] Frisch and Stern, Zeits. f. Physik 85, 4 (1933); Estermann and Stern, Zeits. f. Physik 85, 17 (1933).
- [2] E. Fermi, L. Marshall, Phys.Rev. 72 1139-1146 (1947).
- [3] J.D. Sullivan, Phys. Rev. **D5**, 1732 (1972).
- [4] J. Speth and A.W. Thomas, Adv. Nucl. Phys. 24, 83 (1997).
- [5] P.L. McGaughey, J.M. Moss, and J.C. Peng, Ann. Rev. Nucl. Part. Sci. 49, 217 (1999).
- [6] S. Kumano, Phys. Rep. 303, 183 (1998).
- [7] A.W. Thomas, Phys. Lett. 126B, 97-100 (1983).
- [8] See, for example, Hall A PR01-110 and Hall B LOI-01-001.
- [9] T. J. Hobbs et al., "A study of fracture functions for semi-inclusive electroproduction of low-momentum baryons" (2014, in preparation).
- [10] H. Holtmann, A. Szczurek and J. Speth, Nucl. Phys. **A 596**, 631 (1996).
- [11] W. Melnitchouk and A. W. Thomas, Z. Phys. A **353**, 311 (1995).
- [12] J. D. Sullivan, Phys. Rev. D **5**, 1732 (1972).
- [13] V. R. Zoller, Z. Phys. C **53**, 443 (1992).
- [14] W. Melnitchouk and A. W. Thomas, Phys. Rev. D **47**, 3794 (1993).
- [15] H. Holtmann, A. Szczurek and J. Speth, Nucl. Phys. **A596**, 631 (1996).
- [16] J. Speth and A. W. Thomas, Adv. Nucl. Phys. **24**, 83 (1998).
- [17] S. Kumano, Phys. Rep. **303**, 183 (1998).
- [18] W. Melnitchouk, A. W. Schreiber and A. W. Thomas, Phys. Rev. D **49**, 1183 (1994).
- [19] R. Machleidt, K. Holinde and C. Elster, Phys. Rep. **149**, 1 (1987).
- [20] B. Holzenkamp, K. Holinde and J. Speth, Nucl. Phys. **A500**, 485 (1989).
- [21] D. de Florian and R. Sassot, Phys. Rev. D **56**, 426 (1997) [hep-ph/9703228].
- [22] H. Holtmann, G. Levman, N. N. Nikolaev, A. Szczurek and J. Speth, Phys. Lett. B **338**, 393 (1995) [hep-ph/9602229].
- [23] M. Glück, E. Reya, A. Vogt, Z. Phys. C **53**, 651 (1992).

- [24] A. D. Martin, R. G. Roberts, W. J. Stirling and P. J. Sutton, Phys. Rev. D **45**, 2349 (1992).
- [25] S. Kumano, Phys. Rept. **303**, 183 (1998) [hep-ph/9702367].
- [26] G. T. Garvey and J. -C. Peng, Prog. Part. Nucl. Phys. **47**, 203 (2001) [nucl-ex/0109010].
- [27] M. Gluck, E. Reya and A. Vogt, Eur. Phys. J. C **5**, 461 (1998) [hep-ph/9806404]; M. Gluck, P. Jimenez-Delgado and E. Reya, Eur. Phys. J. C **53**, 355 (2008) [arXiv:0709.0614 [hep-ph]].
- [28] A. D. Martin, W. J. Stirling, R. S. Thorne and G. Watt, Eur. Phys. J. C **63**, 189 (2009) [arXiv:0901.0002 [hep-ph]].
- [29] P. M. Nadolsky, H. -L. Lai, Q. -H. Cao, J. Huston, J. Pumplin, D. Stump, W. -K. Tung and C. -P. Yuan, Phys. Rev. D **78**, 013004 (2008) [arXiv:0802.0007 [hep-ph]].
- [30] D. de Florian, R. Sassot, M. Stratmann and W. Vogelsang, Phys. Rev. D **80**, 034030 (2009) [arXiv:0904.3821 [hep-ph]].
- [31] E. Leader, A. V. Sidorov and D. B. Stamenov, Phys. Rev. D **73**, 034023 (2006) [hep-ph/0512114].
- [32] J. Dudek, R. Ent, R. Essig, K. S. Kumar, C. Meyer, R. D. McKeown, Z. E. Meziani and G. A. Miller *et al.*, “*Physics Opportunities with the 12 GeV Upgrade at Jefferson Lab*,” Eur. Phys. J. A **48**, 187 (2012) [arXiv:1208.1244 [hep-ex]].
- [33] L. Trentadue and G. Veneziano, Phys. Lett. B **323**, 201 (1994).
- [34] J. C. Collins, Phys. Rev. D **57**, 3051 (1998) [Erratum-ibid. D **61**, 019902 (2000)] [hep-ph/9709499].
- [35] G. Baum *et al.* [COMPASS Collaboration], “*COMPASS: A Proposal for a Common Muon and Proton Apparatus for Structure and Spectroscopy*,” CERN-SPSLC-96-14 (1996).
- [36] F. D. Aaron *et al.* [H1 and ZEUS Collaborations], Eur. Phys. J. C **72**, 2175 (2012) [arXiv:1207.4864 [hep-ex]].
- [37] F. D. Aaron, C. Alexa, V. Andreev, S. Backovic, A. Baghdasaryan, E. Barrelet, W. Bartel and K. Begzsuren *et al.*, Eur. Phys. J. C **71**, 1578 (2011) [arXiv:1010.1476 [hep-ex]].
- [38] S. Chekanov *et al.* [ZEUS Collaboration], Nucl. Phys. B **816**, 1 (2009) [arXiv:0812.2003 [hep-ex]].
- [39] F. D. Aaron *et al.* [H1 Collaboration], Eur. Phys. J. C **68**, 381 (2010) [arXiv:1001.0532 [hep-ex]].

- [40] G. Altarelli and G. Parisi, Nucl. Phys. B126 298 (1977).
- [41] ZEUS Collaboration, M. Derrick et al., Phys. Lett. B384 388 (1996).
- [42] L. Trentadue and G. Veneziano, Phys. Lett. B323 201 (1994).
- [43] D. de Florian and R. Sassot, Phys. Rev. D 56 426 (1997).
- [44] H. Holtmann et al., Phys. Lett. B338 363 (1994).
- [45] P. Maris, C. D. Roberts, P. C. Tandy, Phys. Lett. **B420**, 287 (1998).
- [46] J. S. Conway *et al.*, Phys Rev. D **39**, 39 (1989).
- [47] J. Badier *et al.*, Z. Phys. **C18**, 281 (1983).
- [48] B. Betev *et al.*, Z. Phys. **C28**, 9 (1985).
- [49] HI Collaboration, C. Adloff *et al.*, Eur. Phys. J. **C6**, 587 (1999); V. Andreev *et al.*, arxiv:1312.4821.
- [50] G. R. Farrar and D. R. Jackson, Phys. Rev. Lett. **35**, 1416 (1975).
- [51] X. Ji, J.-P. Ma, and F. Yuan, Phys. Lett. **B610**, 247 (2005).
- [52] S. J. Brodsky, M. Burkardt, and I. Schmidt, Nucl. Phys. **B441**, 197 (1995).
- [53] M. B. Hecht, C. D. Roberts, and S. M. Schmidt, Phys. Rev. **C63**, 025213 (2001).
- [54] P. Maris and C. D. Roberts, Int J. Mod. Phys. **E12**, 297 (2003).
- [55] J. C. R. Bloch, C. D. Roberts, S. M. Schmidt, A. Bender, and M. R. Frank Phys Rev. **C60**, 062201 (1999).
- [56] J. C. R. Bloch, C. D. Roberts, and S. M. Schmidt, Phys Rev. **C61**, 065207 (2000).
- [57] T. Frederico and G. A. Miller, Phys. Rev. **D50**, 210 (1994).
- [58] A. Szczepaniak, C.-R. Ji, and S. R. Cotanch, Phys. Rev. **D49**, 3466 (1994).
- [59] T. Shigetani, K. Suzuki, and H. Toki, Phys. Lett. **B308**, 383 (1993).
- [60] R. M. Davidson, and E. Ruiz Arriola, Phys. Lett. **B348**, 163 (1995).
- [61] H. Weigel, E. Ruiz Arriola, and L. P. Gamberg, Nucl. Phys. **B560**, 383 (1999).
- [62] W. Bentz, T. Hama, T. Matsuki, and K. Yazaki, Nucl. Phys. **A651**, 143 (1999).
- [63] S. D. Drell, and T.-M. Yan, Phys. Rev. Lett **24**, 181 (1970).
- [64] G. B. West, Phys. Rev. Lett. **24**, 1206 (1970).
- [65] W. Melnitchouk, Eur. Phys. J. **A17**, 223 (2003).



- [66] K. Suzuki and W. Weise, Nucl. Phys. **A634**, 141 (1998).
- [67] J. D. Sullivan, Phys. Rev. **D 5**, 1732 (1972).
- [68] A. Thomas, Phys. Lett. **B 126**, 97 (1983).
- [69] NMC Collaboration, P. Amaudruz et al, Phys. Rev. Lett. **66**, 2712 (1991); P. Amaudruz *et al.*, Phys. Rev. **D 50**, R1 (1994)
- [70] K. Gottfried, Phys. Rev. Lett. **18**, 1174 (1967).
- [71] A. Baldit *et al.*, Phys. Lett. **B 332**, 244 (1994).
- [72] E866 Collaboration, E. A. Hawker *et al.*, Phys. Rev. Lett. **80**, 3715 (1998).
- [73] E866 Collaboration, J. C. Peng *et al.*, Phys. Rev. **D 58**, 092004 (1998).
- [74] E866 Collaboration, R. S. Towell *et al.*, Phys. Rev. **D 80**, 3715 (1998).
- [75] HERMES Collaboration, K. Akerstaff *et al.*, Phys. Lett. **B 464**, 123 (1999).
- [76]
- [77] S. Kumano, Phys. Rep. **303**, 183 (1998).
- [78] J. P. Speth and A. W. Thomas, Adv. Nucl. Phys. **24**, 83 (1998).
- [79] G. T. Garvey and J. C Peng, Prog. Part. Nucl. Phys. **47**, 203 (2001).
- [80] Nikolaev *et al.*, Phys. Rev. **D60**, 014004 (1999).
- [81] B. Kopeliovich and B. Povh, Z. Phys. C **73**, 125 (1996).
- [82] U. D' Alesio and H. J. Pirner Eur. Phys. J. A **7**, 109 (2000).
- [83] V. Stoks Nucl. Phys. A **629**, 205c (1998); V. Stoks and Th. A. Rijken, Phys. Rev. C **59**, 3009 (1999).
- [84] H. Hoffmann et al., Phys. Lett. **B 338**, 363 (1994).
- [85] M. Gluck, E. Reya, A. Vogt, Z. Phys. **C 53**, 651 (1992).
- [86] CERNLIB PDFLIB version 8.04.
- [87] M. Gluck, E. Reya, A. Vogt, Z. Phys. **C 67**, 433 (1995).
- [88] see, for example, Review of Particle Physics - Particle Data Group Collaboration (Beringer, J. et al.) Phys.Rev. D86 (2012) 010001 and M. R. Whalley, Comput. Phys. Commun. **57**, 536 (1989).
- [89] T. Hobbs, W. Melnitchouk, private communication
- [90] F. Sauli, Nucl. Instrum. Meth. **A386**, 531 (1997).

- [91] Gianfranco Morello, talk at Exploring Hadron Structure with Tagged Structure Functions workshop at Jefferson Lab (2014).
- [92] S.K. Das *et al.*, Nucl. Instrum. Meth. A **625**, 39-42 (2011).
- [93] L. W. Whitlow, E. M. Riordan, S. Dasu, S. Rock and A. Bodek, Phys. Lett. B **282**, 475 (1992).
- [94] S. Tkachenko *et al.* [CLAS Collaboration], Phys. Rev. C **89**, 045206 (2014).
- [95] D.E. Wiser, Ph.D. Thesis, University of Wisconsin-Madison (1977) (unpublished).
- [96] B. A. Mecking *et al.*, Nucl. Inst. and Meth. **A503**, 513 (2003).
- [97] V. Sapunenko, *et al.*, Nucl. Instr. and Meth. A, to be submitted.